

Mass Reconstruction of Galaxy-scale Strong Gravitational Lenses Using Broken Power-law Model

WEI DU,^{1,*} LIPING FU,^{1,†} YIPING SHU,² RAN LI,^{3,4,5} ZUHUI FAN,⁶ AND CHENGGANG SHU¹

¹Shanghai Key Lab for Astrophysics, Shanghai Normal University, Shanghai, 200234, China

²Purple Mountain Observatory, Chinese Academy of Science, Nanjing, 210023, China

³National Astronomical Observatories, Chinese Academy of Science, Beijing, 100101, China

⁴Institute for Frontiers in Astronomy and Astrophysics, Beijing Normal University, Beijing, 102206, China

⁵School of Astronomy and Space Science, University of Chinese Academy of Sciences, Beijing, 100049, China

⁶South-Western Institute for Astronomy Research, Yunnan University, Kunming, 650500, China

ABSTRACT

With mock strong gravitational lensing images, we investigate the performance of broken power-law (BPL) model on the mass reconstruction of galaxy-scale lenses. An end-to-end test is carried out, including the creation of mock strong lensing images, the subtraction of lens light, and the reconstruction of lensed images. Based on these analyses, we can reliably evaluate how accurate the lens mass and source light distributions can be measured. We notice that, based on lensed images alone, only the Einstein radii (R_E) or the mean convergence within them can be well determined, with negligible bias (typically $< 1\%$) and controllable uncertainty. Away from the Einstein radii, the radial and mean convergence profiles can hardly be constrained unless well-designed priors are applied to the BPL model. We find that, with rigid priors, the BPL model can clearly outperform the singular power-law models by recovering the lens mass distributions with small biases out to several Einstein radii (*e.g.*, no more than 5% biases for the mean convergence profiles within $3 R_E$). We find that the source light reconstructions are sensitive to both lens light contamination and lens mass models, where the BPL model with rigid priors still performs best when there is no lens light contamination. It is shown that, by correcting for the projection effect, the BPL model is capable of estimating the aperture and luminosity weighted line-of-sight velocity dispersions to an accuracy of $\sim 6\%$. These results further highlight the great potential of the BPL model in strong lensing related studies.

Keywords: dark matter — galaxies: halos — galaxies: kinematics and dynamics — gravitational lensing: strong

1. INTRODUCTION

Strong gravitational lensing (SL) has proven to be an important tool to learn about the universe because of its sensitivity to the geometry of the universe and the matter distribution therein, for example, by constraining cosmological parameters (Jullo et al. 2010; Collett et al. 2012; Cao et al. 2015; Linder 2016), testing gravity (Bolton et al. 2006; Koopmans et al. 2009; Collett et al. 2018) and measuring the mass distribution of intervening objects (Shu et al. 2008; Coe et al. 2012; Gomer & Williams 2020; Chen et al. 2022). In addition, SL can magnify the distant galaxies and help us look into

their properties in more detail (*e.g.*, Marshall et al. 2007; Newton et al. 2011).

In recent years, one of the most attention-getting measurements from SL observations is the constraint on Hubble constant H_0 using time-delay cosmography (Suyu et al. 2013; Bonvin et al. 2017; Wong et al. 2020; Shajib et al. 2020). For instance, the H_0 Lenses in COSMOGRAIL’s Wellspring (H0LiCOW) collaboration found $H_0 = 73.3^{+1.7}_{-1.8} \text{ km s}^{-1} \text{ Mpc}^{-1}$ from a joint analysis of six time-delay systems (Wong et al. 2020), in 3.1σ tension with Planck observations of the cosmic microwave background. Based on a single time-delay system with two sets of multiple images at different redshifts, Shajib et al. (2020) reported a 3.9 percent measurement of H_0 . In light of these reported precisions, we have high hope of achieving 1 percent precision in H_0 using tens of time-delay systems.

* E-mail: duwei@shnu.edu.cn

† E-mail: fulip@shnu.edu.cn

However, there is much debate over these reported high precisions of H_0 measurements, because there exist many lensing degeneracies making it very difficult to accurately recover the mass distributions along the line-of-sight (LoS) (*e.g.* Schneider & Sluse 2013, 2014; Xu et al. 2016; Sonnenfeld 2018; Kochanek 2020, 2021; Millon et al. 2020). Inaccurate reconstruction of the lensing mass distributions, especially the main lens which dominates the lensing potential along the LoS, may lead to uncontrollable systematics in H_0 estimation.

Among the lensing degeneracies, the most famous one is the mass-sheet degeneracy (MSD, Falco et al. 1985), which indicates the lensed images produced by a convergence profile $\kappa(\theta) + \kappa_{\text{ext}}$ can be totally recovered by a transformed profile $(1 - \kappa'_{\text{ext}})\kappa(\theta)/(1 - \kappa_{\text{ext}}) + \kappa'_{\text{ext}}$ with a corresponding rescaling of the source plane, where $\kappa(\theta)$, κ_{ext} and κ'_{ext} represent the convergence profiles of the main lens, the actual external convergence and a guess about κ_{ext} , respectively. Since external convergence is not a direct observable, it is usually very hard to quantify with high accuracy (Treu et al. 2009; Suyu et al. 2010; Guimarães & Sodré 2011; Tikhonova et al. 2020), thus leading to large uncertainties in the determination of mass distributions and thus H_0 .

The MSD, as we know, is a special case of the source-position transformation (SPT, Schneider & Sluse 2014). The SPT refers to the fact that different combinations of lens mass and source light distributions can produce very similar or indistinguishable lensed images (Schneider & Sluse 2013; Unruh et al. 2017). Schneider & Sluse (2013) illustrated the impact of SPT on the determination of H_0 , and showed that the predicted H_0 can deviate by $\sim 20\%$ if the lensed images produced by a composite lens are fitted by the singular power-law (SPL) model.

In addition to the MSD or SPT, there are more lensing degeneracies, such as the monopole degeneracy in regions without lensed images (Saha 2000; Liesenborgs & De Rijcke 2012) and the local degeneracies just around the lensed images (Gorenstein et al. 1988; Wagner 2018). These degeneracies can bring about more uncertainties in the determination of lens mass distributions as well as H_0 . Actually, not only H_0 , but many other quantities relevant to SL analyses, *e.g.*, cosmological distance ratios and parameterized post-Newtonian parameter γ_{PPN} (Bolton et al. 2006; Schwab et al. 2010), are vulnerable to the above mentioned lensing degeneracies.

In view of these degeneracies, a question arises about what quantities can be determined faithfully by lensed images. Usually, the Einstein radius is deemed to be such a quantity (Schneider et al. 2006; Treu 2010). Its measurement error is typically of the order of a few per-

cent (Bolton et al. 2008; Shu et al. 2015, 2016; Shajib et al. 2021; Etherington et al. 2022). However, there are also works showing surprising results. Recently, based on simulated SL systems with mass distributions inferred from SDSS-MaNGA stellar dynamics data (Li et al. 2019), Cao et al. (2022) concluded that the Einstein radius can be recovered with 0.1% accuracy. On the other hand, Mukherjee et al. (2018) found a large scatter of $\sim 20\%$ in Einstein radius estimation when comparing SIE model fittings to the direct convergence fittings, where the mock lensed images are created using galaxies from EAGLE simulations (Schaye et al. 2015).

The other quantity, which can be constrained independently of lens mass models, is $\xi_2 = R_E \alpha''_E / (1 - \kappa_E)$, where α''_E is the second-order radial derivative of the deflection profile at Einstein radius R_E and κ_E is the convergence at R_E (Sonnenfeld 2018; Kochanek 2020, 2021; Birrer 2021). For axisymmetric or moderate elliptical lenses, R_E and ξ_2 are the two parameters that lensed images can constrain reliably. Sonnenfeld (2018) argued that, in order to avoid over-constraining the lens mass distributions, a lens model should have at least 3 degrees of freedom in the radial direction. The SPL model with only two radial parameters should be abandoned if higher accuracies are needed in the determination of cosmological parameters, as suggested by Kochanek (2020).

Nevertheless, only when lens mass distributions are reconstructed more accurately, can the relevant cosmological parameters be estimated more reliably. In SL analyses, a lens model is preferred if its deflection field can be computed analytically. Many spherical models meet this requirement (see a list of lens models shown in Keeton 2001), while only a handful of elliptical models have analytic expressions for deflections, *e.g.*, softened power-law (Wertz & Surdej 2014), three-dimensional broken power-law (BPL, Du et al. 2020) and two-dimensional BPL (O’Riordan et al. 2021) models. The commonly adopted singular isothermal ellipsoid (SIE, Kassiola & Kovner 1993; Keeton & Kochanek 1998) and SPL models (Tessore & Metcalf 2015) are the special cases of the above mentioned elliptical models.

Among the analytical lens mass models, the BPL model proposed by Du et al. (2020) is a flexible model with four degrees of freedom in the radial direction which can describe not only the mass distributions of lenses with flat cores, but also with steep cusps. Furthermore, it can also fit well the well-known NFW (Navarro et al. 1997) and Einasto (Einasto 1965) profiles within sufficiently large radii. In this paper, we concentrate on this BPL model and, based on simulated SL systems, look into how accurate the lens mass distributions can be recovered by fitting the lensed images.

The rest of this paper is organized as follows. In Section 2, we briefly review the basics about BPL model. In Section 3, we show the creation of mock lensing observations, which are used to evaluate the BPL model as well as the SIE and SPL models. We describe in detail the extraction and reconstruction of lensed images in Section 4 and investigate the necessary priors in lens mass modeling. Results are presented in Section 5. Conclusion and discussions are given in the last section.

2. THE BPL MODEL

In this section, we briefly review the basics about the BPL model, including its density profiles and deflections. We also show the formalism for estimating the line-of-sight velocity dispersions (LOSVDs) observed by single-fiber spectroscopy, *i.e.*, the aperture and luminosity (AL) weighted LOSVDs which provide importantly the dynamical information for calibrating the lensing mass distributions.

2.1. The volume and surface density profiles

The volume density profile of BPL model is expressed by

$$\rho(r) = \begin{cases} \rho_c (r/r_c)^{-\alpha_c} & \text{if } r \leq r_c \\ \rho_c (r/r_c)^{-\alpha} & \text{if } r \geq r_c, \end{cases} \quad (1)$$

where α_c and α are respectively the inner and outer slopes, and ρ_c is the volume density at break radius r_c .

By integrating $\rho(r)$ along the line-of-sight, one obtains the surface mass density profile $\Sigma(R)$, and then has the convergence profile $\kappa(R) = \Sigma(R)/\Sigma_{\text{crit}}$ with

$$\Sigma_{\text{crit}} = \frac{c^2}{4\pi G} \frac{D_s}{D_d D_{ds}} \quad (2)$$

known as the critical surface mass density in lensing analyses, where D_d , D_s , and D_{ds} are the angular diameter distances to the lens deflector, to the source, and from the deflector to the source, respectively.

As shown by Du et al. (2020), $\kappa(R)$ can be expressed in terms of two parts as

$$\kappa(R) = \kappa_1(R) + \kappa_2(R), \quad (3)$$

with

$$\kappa_1(R) = \frac{3-\alpha}{2} \left(\frac{b}{R} \right)^{\alpha-1} \quad (4)$$

corresponding to a single power-law part and

$$\kappa_2(R) = \frac{3-\alpha}{\mathcal{B}(\alpha)} \left(\frac{b}{r_c} \right)^{\alpha-1} \times \tilde{z} \left[F \left(\frac{\alpha_c}{2}, 1; \frac{3}{2}; \tilde{z}^2 \right) - F \left(\frac{\alpha}{2}, 1; \frac{3}{2}; \tilde{z}^2 \right) \right] \quad (5)$$

a complementary part within r_c , which is a mass deficit for $\alpha_c < \alpha$ or a mass surplus for $\alpha_c > \alpha$, where $\mathcal{B}(\alpha) = \text{Beta}(\frac{1}{2}, \frac{\alpha-1}{2})$, $\tilde{z} = \sqrt{1 - R^2/r_c^2}$, $F()$ denotes the Gauss hypergeometric function and b is a scale radius defined by

$$b^{\alpha-1} = \frac{\mathcal{B}(\alpha)}{\Sigma_{\text{crit}}} \frac{2}{3-\alpha} \rho_c r_c^\alpha. \quad (6)$$

Note that $\kappa_2(R)$ is zero when $R \geq r_c$ or $\alpha_c = \alpha$.

In order to describe surface mass distributions which are elliptically symmetric, the circular radius R in $\kappa(R)$ can be generalized to elliptical radius $R_{\text{el}} = \sqrt{qx^2 + y^2/q}$, where q is the axis ratio of the elliptical isodensities. In this case, the area enclosed by R_{el} is πR_{el}^2 independent of q . In view of this advantage, we thus can define an effective Einstein radius of a lens as the elliptical radius within which the mean convergence is unity.

2.2. The deflection angles

In complex notation, the lens equation is

$$z_s = z - \alpha(z), \quad (7)$$

which relates the true source position $z_s = x_s + iy_s$ on source plane to its observed position $z = x + iy$ on lens plane (Please do not confuse the complex numbers z in this subsection with the redshift symbols in other sections), where $\alpha(z) = \alpha_x + i\alpha_y$ is the scaled deflection angle caused by the intervening lens (Schneider et al. 2006; Tessore & Metcalf 2015). If the lens mass distribution is elliptically symmetric, the deflection angle $\alpha(z)$ at position z can be evaluated by

$$\alpha^*(z) = \frac{2}{z} \int_0^{R_{\text{el}}} \frac{\kappa(R)R \, dR}{\sqrt{1 - \zeta^2 R^2}}, \quad (8)$$

where the symbol $*$ denotes the complex conjugate, $\zeta^2 = (1/q - q)/z^2$ and R_{el} is the elliptical radius of the ellipse passing through the position z (Bourassa & Kantowski 1975; Bray 1984).

As presented in Du et al. (2020), by substituting Equation (3) into Equation (8), we have the deflections $\alpha^*(z) = \alpha_1^*(z) + \alpha_2^*(z)$ for the BPL model, with

$$\alpha_1^*(z) = \frac{R_{\text{el}}^2}{z} \left(\frac{b}{R_{\text{el}}} \right)^{\alpha-1} F \left(\frac{1}{2}, \frac{3-\alpha}{2}; \frac{5-\alpha}{2}; \zeta^2 R_{\text{el}}^2 \right) \quad (9)$$

for the power-law part κ_1 and

$$\alpha_2^*(z) = \frac{r_c^2}{z} \frac{3-\alpha}{\mathcal{B}(\alpha)} \left(\frac{b}{r_c} \right)^{\alpha-1} \left[\frac{2}{3-\alpha_c} \mathcal{F} \left(\frac{3-\alpha_c}{2}, \mathcal{C} \right) - \frac{2}{3-\alpha} \mathcal{F} \left(\frac{3-\alpha}{2}, \mathcal{C} \right) - \mathcal{S}_0(\alpha, \alpha_c, \tilde{z}_{\text{el}}, \mathcal{C}) \right] \quad (10)$$

for the complementary part κ_2 , where $\mathcal{C} = r_c^2 \zeta^2$, $\tilde{z}_{\text{el}} = \sqrt{1 - R_{\text{el}}^2/r_c^2}$, and functions \mathcal{F} and \mathcal{S}_0 can be written in terms of the Gauss hypergeometric functions¹. Please refer to the subsection 2.2 in Du et al. (2020) for detailed expressions of \mathcal{F} and \mathcal{S}_0 . Note that \mathcal{S}_0 disappears when $R_{\text{el}} \geq r_c$ or $\alpha_c = \alpha$.

2.3. The AL-weighted LOSVDs

In addition to testing the accuracy of mass measurements of galaxy-scale lenses, we are also interested in the accuracy of AL-weighted LOSVDs predicted from the reconstructed mass distributions, which can help us calibrate the lens mass distributions.

As we know, based on the spherical Jeans equation, the AL-weighted LOSVD for a galaxy with constant velocity anisotropy can be modeled as

$$\langle \sigma_{\parallel}^2 \rangle = \frac{\int_0^{\infty} dR \, R w(R) \int_{-\infty}^{\infty} dZ \, j(r) (1 - \beta R^2/r^2) \sigma_r^2(r)}{\int_0^{\infty} dR \, R w(R) \int_{-\infty}^{\infty} dZ \, j(r)} \quad (11)$$

where $\sigma_r^2(r)$ is the radial velocity dispersion for stars, β denotes the global velocity anisotropy, $j(r)$ is the 3D luminosity density profile, and $w(R)$ is a weighting function accounting for the fiber size and seeing effect for ground-based spectroscopic observations.

By assuming $w(R)$ follows a Gaussian distribution (Schwab et al. 2010), *i.e.*,

$$w(R) \approx \exp\left(-\frac{R^2}{2\sigma_{\text{fib}}^2}\right), \quad (12)$$

where σ_{fib} is a function of seeing and fiber size, Du et al. (2020) found that Equation (11) can be transformed into

$$\langle \sigma_{\parallel}^2 \rangle = \frac{\int_0^{\infty} dr \, r^2 j(r) \sigma_r^2(r) \left[\Phi\left(1, \frac{3}{2}; -\frac{r^2}{2\sigma_{\text{fib}}^2}\right) - \frac{2\beta}{3} \Phi\left(2, \frac{5}{2}; -\frac{r^2}{2\sigma_{\text{fib}}^2}\right) \right]}{\int_0^{\infty} dr \, r^2 j(r) \Phi\left(1, \frac{3}{2}; -\frac{r^2}{2\sigma_{\text{fib}}^2}\right)} \quad (13)$$

with only 1D integrals, where $\Phi(a_1, a_2; -x)$ is the Kummer's confluent hypergeometric function.

We adopt the power-law Sérsic (PL-Sérsic) profile to describe the light (or stellar mass) density profiles (Terzić & Graham 2005), which is written as

$$j(r) = \begin{cases} j_c (r/r_c)^{-\alpha_c} & \text{if } r \leq r_c \\ j_0 \left(\frac{r}{s}\right)^{-u} \exp\left[-\left(\frac{r}{s}\right)^{\nu}\right] & \text{if } r \geq r_c \end{cases} \quad (14)$$

¹ In this paper, the Gauss hypergeometric function is computed using the function `scipy.special.hyp2f1` in Python, where the latest version of SciPy library is recommended since it solves the divergence problem of function `hyp2f1` in some regions.

where

$$j_0 = j_c \left(\frac{r_c}{s}\right)^u \exp\left[\left(\frac{r_c}{s}\right)^{\nu}\right], \quad (15)$$

j_c is the luminosity density at break radius r_c , $s = R_{\text{eff}}/k^n$ is a scale radius defined by the 2D effective radius R_{eff} for the Sérsic profile and the Sérsic index n (k here is a function of n and its expression can be found in Ciotti & Bertin 1999 and MacArthur et al. 2003), $\nu = 1/n$, and $u = 1 - 0.6097\nu + 0.054635\nu^2$ (Lima Neto et al. 1999; Márquez et al. 2001).

Given the BPL mass model and PL-Sérsic light profile, the radial velocity dispersion $\sigma_r^2(r)$ can be analytically calculated. Please refer to the Equations (41)-(45) in Du et al. (2020) for the analytical expressions of $\sigma_r^2(r)$, where the PL-Sérsic profile is assumed to have the same break radius r_c and inner slope α_c as the BPL model.

3. MOCK LENSING OBSERVATIONS

In this section, we first display some basics about observed SL systems which are used for reference, and then briefly describe the Illustris simulation from which a sample of galaxies are selected as mock lenses. In the third subsection, we show the generation of hundreds of mock SL systems with single or multiple exposures.

3.1. Observational data

In order to produce realistic lensing images, we refer to the lenses detected by the Sloan Lens ACS (SLACS) and the SLACS for the mass (S4TM) surveys (Bolton et al. 2008; Shu et al. 2015). The SL candidates for these two surveys are first identified by taking advantage of the galaxy spectra from SDSS. And then, follow-up imaging observations are performed with the Advanced Camera for Surveys (ACS) aboard the Hubble Space Telescope (HST).

By visually inspecting the high resolution HST images, the SL candidates are classified into different classes, where the ones with clear and definite lensing features are termed “grade-A” lenses. In the following analyses, we use the grade-A systems with only one dominant lens for reference. In total, we have 63 SLACS lenses (20 with one exposure and 43 with multiple exposures) and 38 S4TM lenses (all with one exposure), most of which are elliptical galaxies. Hereafter, we refer to both SLACS and S4TM surveys simply as SLACS surveys.

Shu et al. (2015) estimated the stellar masses of these lenses by scaling single stellar population models to fit their HST F814W photometry. It is thus expected that a scaling relation may exist between the observed total number of photon-excited electrons N_e and stellar masses M_{\star} for these lenses. By adopting the favored stellar masses inferred with the Chabrier stellar initial

mass function (Chabrier 2003), we find the N_e can be connected with the M_\star simply by

$$N_e \approx \frac{0.2M_\star}{4\pi D_L^2(1+z)^{0.5}} e^-/s, \quad (16)$$

where D_L is the luminosity distance in units of Mpc and M_\star is in units of M_\odot . Using this scaling relation, we thus can assign a total number of electrons to a lens galaxy to mimic HST-like observations in an easy way.

Figure 1 illustrates some basic information about the 101 lenses (63 SLACS and 38 S4TM lenses). The left panel shows the redshift distribution of the lenses. The middle panel presents the stellar mass distribution of the real lenses (black histogram) and mock lenses (red histogram). The last panel illustrates the perfect fitting of Equation (16) to the ratio of N_e and M_\star as a function of redshift.

3.2. The Illustris simulation

The Illustris project runs a set of large-scale hydrodynamic simulations by accounting for various kinds of baryonic physics including gas cooling; star formation and evolution; feedback from active galactic nuclei, supernovae and supermassive black holes; and so on (Genel et al. 2014; Vogelsberger et al. 2014; Nelson et al. 2015). It assumes a flat Λ CDM cosmology with $\Omega_m = 0.2726$, $\Omega_\Lambda = 0.7274$, $\Omega_b = 0.0456$, $\sigma_8 = 0.809$, $n_s = 0.963$ and $h = 0.704$. Among the simulation runs, the one with the highest resolution is named as the Illustris-1 simulation from which we extract massive galaxies to generate mock SL systems.

Specifically, the Illustris-1 simulation follows 1820^3 dark matter particles and initially 1820^3 hydrodynamical cells in a periodic box of size $75 h^{-1}\text{Mpc}$. The mass for a dark matter particle is $\sim 6.26 \times 10^6 M_\odot$, and the baryonic matter has an initial mass resolution of $\sim 1.26 \times 10^6 M_\odot$. At the end of the simulation, the minimum mass for a baryonic matter particle reaches to a few times $10^4 M_\odot$. The simulation assigns different softening lengths to different types of particles. For example, the softening length is fixed to be a comoving value of $1 h^{-1}\text{kpc}$ for dark matter particles and is larger than $0.5 h^{-1}\text{kpc}$ in physical scale for stars and black holes. For gas cells, an adaptive softening length is defined according to the fiducial cell size, with a minimum equaling to that used for the collisionless baryonic particles.

3.3. Generation of mock observations

Using the Illustris-1 simulation at redshift zero, we extract 5343 galaxies with stellar mass larger than $10^{10} h^{-1}M_\odot$. These galaxies are artificially put at redshift $z_d \simeq 0.178$ which is close to the median redshift

of the SLACS lenses (see the vertical dashed line shown in the left panel of Figure 1). At this redshift, $1''$ corresponds to 3 kpc for the cosmology adopted by the Illustris project.

Based on thin lens approximation, we project the 3D mass distributions of the galaxies along the x -direction of the simulation box onto the 2D lens plane at $z_d \simeq 0.178$ to analyze their lensing effect. In the process of projection, all the matter components are considered including the dark matter, stars, gas, and black holes. We assume the source plane is at redshift $z_s = 0.6$ which is around the median redshift of the background sources of the SLACS lensing systems. In this case, the critical surface mass density is $\Sigma_{\text{crit}} \simeq 4.0 \times 10^{15} M_\odot/\text{Mpc}^2$ for the Illustris-adopted cosmology.

We define the “true” Einstein radius for each galaxy as the radius of a circle within which the mean convergence is unity. Based on these true Einstein radii, we find that only a small fraction of galaxies can produce noticeable lensed images. For example, there are only ~ 350 galaxies whose Einstein radii are larger than $0''.5$. With the purpose of generating SL systems whose statistics are similar to those of the SLACS survey, we choose 283 galaxies with Einstein radii in the range of $0''.6$ to $2''$ as the main sample for further analyses, of which about 85% are elliptical galaxies.

Based on the 283 galaxies, we first pixelize their projected overall and stellar mass distributions using the triangular shaped cloud algorithm (Hockney & Eastwood 1981), respectively, with a resolution of $0''.05$. We then get 283 convergence maps by scaling the projected overall mass density distributions with Σ_{crit} . By resorting to Equation (16) and assuming a constant mass-to-light ratio, the light distributions in units of e^-/s can thus be derived for the lenses from their stellar mass distributions.

As we know, the deflection angle can be expressed as a convolution product between the convergence map $\kappa(\vec{x})$ and the kernel $\vec{x}/|\vec{x}|^2$. Given a surface mass distribution sampled in a regular grid, it is easy to derive the deflection field in Fourier space by applying the convolution theorem. For the 283 galaxy lenses, their deflection angles at grid points are thus evaluated in this way, where the FoV of the convergence map for each lens is large enough to cover its entire halo with zero-padding. By tracing the light rays back to the source plane based on the lens equation, we can construct lensed images of background sources. SL images without photometric noise can thus be obtained by directly adding together the light distributions of foreground galaxies and lensed images.

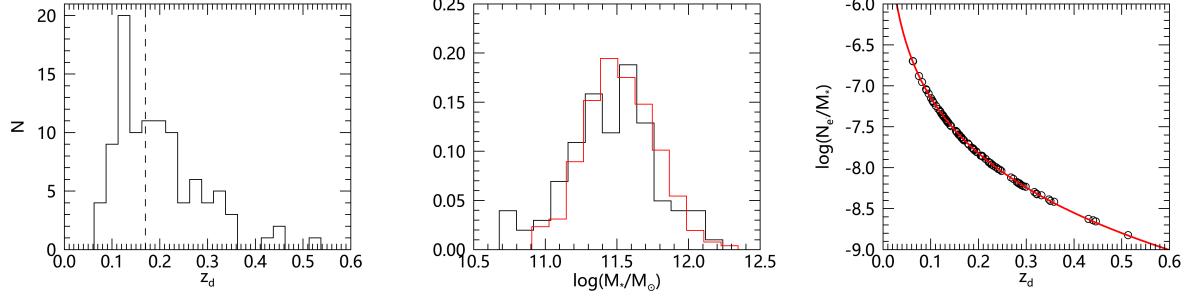


Figure 1. Some basic information about 101 reference lenses (63 SLACS and 38 S4TM lenses). Left: the distribution of lens redshift z_d . The vertical dashed line indicates the median redshift of the lenses. Middle: the normalized stellar mass function of the 101 real lenses (black histogram) and the 257 “grade-A” mock lenses (red histogram). Right: the ratio of N_e and M_* as a function of redshift, with the red line corresponding to the prediction from Equation (16).

In this paper, we assume each background source is a faint and compact galaxy which follows a 2D Sérsic profile $I(R) = I_0 \exp \left[-k \left(\frac{R}{R_{\text{eff}}} \right)^n \right]$ with $I_0 = 0.5 \text{ e}^-/\text{s}/\text{pixel}$, $R_{\text{eff}} = 0''.15$ (about 1kpc at redshift $z_s = 0.6$) and Sérsic index $n = 1$. In this case, the corresponding apparent magnitude is ~ 23.5 for the background sources. The properties of source galaxies considered here are roughly consistent with those found by [Newton et al. \(2011\)](#).

More specifically, the position angle of each source galaxy is randomly assigned in the range of 0 to π and its axis ratio is in the range of 0.2 to 1. We randomly place a source galaxy on the source plane around the center of the foreground lens with a scatter of $0''.2$ in both x and y directions. A lensed image will be a candidate while its magnification is larger than 5 and the number of pixels in the feature mask is more than 500 after a certain number of trials. The feature mask is defined in the absence of photometric noises. A pixel in the lensing image is marked as a masked pixel if its light intensity is 5% brighter than that of the lens itself. It is found that the feature mask defined in this way is roughly consistent with (or somewhat larger than) the region visually identified for the lensing features. That is, in practice, we cannot determine the feature mask so straightforwardly because we do not know exactly the true lensed images due to the existence of lens light contamination.

With the aim of producing more realistic lensing images, photometric noises are considered, *e.g.*, a sky background of $0.11 \text{ e}^-/\text{s}$ and the Poisson noise on each pixel. The effect of the point spread function (PSF) is also taken into account by randomly applying the PSF in SLACS images to mock images. Bad pixels due to cosmic rays are added according to the bad pixel distributions in HST images. We also account for a readout noise of 5 e^- for each pixel. By default, the exposure time is 420 s for each lensing image, corresponding to the single exposure time of the SLACS survey. For comparisons,

we also generate SL images with four exposures (2200 s in total). The left panels of Figure 2 shows two examples of mock SL images with a single exposure.

It should be mentioned that, owing to the existence of large flat cores of Illustris galaxies arising from the softening effect in numerical simulations, most of the pure lensed images in our mock catalog exhibit lensing features in or toward the lens centers. This may not be the case for real SL images. Furthermore, due to the contamination of foreground lens light, the central images may disappear or hardly be detected in the lensing images. The missing of central images may preclude the accurate measurements of inner density profiles.

Based on the kinematics of stellar particles, [Du et al. \(2020\)](#) have calculated the AL-weighted LOSVDs for the Illustris galaxies adopted here, where the galaxies are assumed to be at redshift $z_d = 0.178$ and observed by SDSS-like spectroscopy with a fiber radius of $1''.5$ and in a seeing condition of $1''.69$. We take the AL-weighted LOSVDs evaluated by [Du et al. \(2020\)](#) directly as true values in the following analyses.

4. LENSING MASS RECONSTRUCTION

This section includes two parts. One is for the subtraction of foreground lens light distributions using the B-spline technique, and the other is for the reconstruction of lensed images, where priors on mass distributions are investigated in detail.

4.1. Subtraction of lens galaxy light

For most of galaxy-scale lenses, their Einstein radii are typically smaller than their half-light radii, making it difficult to clearly identify the relatively faint lensed images. In order to subtract the foreground light distributions, parametric light profiles, *e.g.*, Sérsic or double Sérsic profiles ([Bolton et al. 2008; Shajib et al. 2019; Birrer et al. 2020; Etherington et al. 2022](#)), are usually adopted as fitting models. However, these profiles with

a limited number of parameters may result in undesired residuals, especially for the light distributions with complex angular structures.

In this paper, we use the B-spline technique, which is a more general model first investigated by [Bolton et al. \(2006\)](#), to fit the foreground light distributions. The B-spline fitting model can be written as

$$I_{\text{bsp}}(R_{\text{el}}, \theta) = \sum_{m,k} [b_{mk} \cos(m\theta) + c_{mk} \sin(m\theta)] f_k(R_{\text{el}}), \quad (17)$$

where $f_k(R_{\text{el}})$ are the radial basis functions with elliptical radius R_{el} , and m denotes the multipole orders in the θ -direction. b_{mk} and c_{mk} are the coefficients which can be determined by fitting the light distributions in a sense of least-squares.

For the B-spline technique, the lensing features need to be estimated and masked in advance so as to get unbiased fittings to the lens light distributions (see Section 3.3 for the definition of feature mask). By masking the estimated lensing features, we then fit the monopole term (*i.e.*, $m = 0$) of light distributions to estimate their centers, ellipticities and position angles. With the centers, ellipticities and position angles fixed, the light distributions are fitted again by adding higher order even multipoles with $m = [2, 4, 6, 8]$. If there are obvious odd features left in the residual for a lens after subtracting the even multipoles, we will further add the odd terms with $m = [1, 3, 5, 7]$ to fit the lens light distribution once more. If the extracted lensing features cannot be clearly recognized no matter what types of multipole terms are included, the corresponding lens systems will be discarded.

Finally, we have 257 “grade-A” lenses left for the single exposure catalog, where 18 lenses show more clear lensing features if the odd multipole terms are included in the B-spline fittings. For the mock catalog with four exposures, we almost have the same cases left, indicating that more exposures may not help us identify more “grade-A” galaxy-scale lenses, because of the significant contamination from foreground lens light. We thus use these 257 lenses with both single and multiple exposures in the following analyses.

Figure 2 shows two examples of B-spline fittings to the single exposure images. The first column displays the SL images with foreground lens light distributions. It is noticed that, for galaxy-scale lenses, the foreground lens light may blur the lensed images significantly and make it difficult to predefine the feature mask. The second column shows the residuals after subtracting the monopole ($m = 0$) term of light distributions. We can see obvious angular structures for these two lenses. By further subtracting the even terms, as shown in the third column,

angular structures almost disappear for the first lens. However, there still exists noticeable odd features for the second lens, which can be largely reduced by further accounting for the odd terms in the B-spline fitting, as demonstrated by the fourth column. For reference, we show in the last column the true lensing features convolved with PSF. It is found that, for these two examples, the extracted lensing features are fairly consistent with the true ones.

4.2. Reconstruction of lensed images

4.2.1. χ^2 definition

In this paper, we use the forward modeling to reconstruct the lensed images, *i.e.*, modeling the lens mass distributions by the BPL model and the source light distributions by the Sérsic profile. For comparisons, the SIE and SPL lens mass models are also investigated.

The χ^2 for the fittings to the extracted lensing features is defined according to

$$\chi^2 = \frac{\sum_{i=1}^N (I_{\text{data}} - I_{\text{bsp}} - I_{\text{model}})_i^2 w_i^2}{\frac{1}{N'} \sum_{j=1}^{N'} (I_{\text{data}} - I_{\text{bsp}})_j^2 w_j^2}, \quad (18)$$

where I_{data} , I_{bsp} and I_{model} denote the light distribution of “observed” lensing image, the B-spline fitting to the foreground light and the modeling of the lensed image convolved with PSF, respectively. The index i indicates the i -th pixel in a suitable field of view and j is for the pixels adopted for the B-spline fittings which do not take into account pixels in feature mask. The w is the reciprocal of the poisson noise error, which is proportional to the square root of the total exposure time in a pixel. Note that, for single exposure images, null weights are assigned to the bad pixels. In order to avoid possible over- or under-fittings of the B-spline technique, the denominator in Equation (18) is applied to scale the weight for each pixel systematically and to make the χ^2 definition reasonable.

We employ the Python module emcee, an affine invariant Markov chain Monte Carlo (MCMC) Ensemble sampler, to estimate the optimal values of parameters ([Foreman-Mackey et al. 2013](#)). The natural logarithm of the posterior probability used for emcee is defined to be

$$\ln \mathcal{P}(\Theta | I_{\text{data}}) = -\frac{1}{2} \chi^2 + \ln p(\Theta) + \text{Const.} \quad (19)$$

where $p(\Theta)$ is the prior function for a set of parameters.

In order to avoid possible local maxima in parameter space, we run twice the MCMC samplings. The first run aims to find an initial guess of the parameters for the

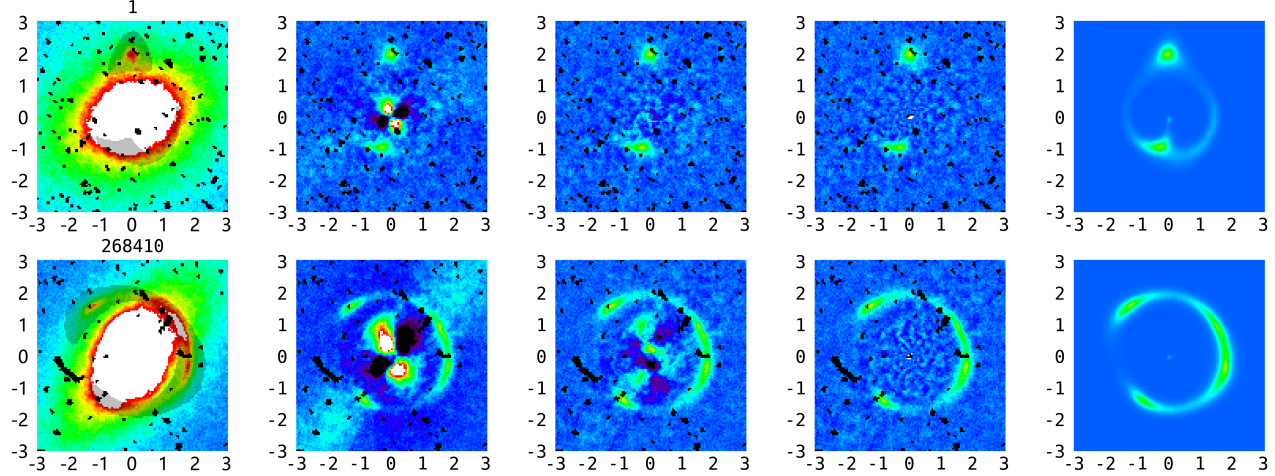


Figure 2. Two examples of extracting lensing features based on the B-spline technique. Shown here for each lens is the central region in the FoV of $6'' \times 6''$. The top and bottom rows are for the lenses with id = 1 and 268410, respectively. The left panels show the lensing images with lens light distributions. The shadows mark the estimated region of lensed images. The second and third columns present the residual images after subtracting the B-spline fittings with monopole and even multipole terms, respectively. The fourth column shows the residual images by further subtracting the possible odd multipole terms. The rightmost column displays the intrinsic lensing features convolved with PSF. Note that, the resolution for all these maps is $0''.05$ and the bad pixels are caused by cosmic rays.

second run, which are taken to be the values resulting in the maximum posterior probability in the first run. For both runs, a large enough number of burn-in steps with 500 walkers are set up to make sure the remaining samplings are in equilibrium. After the second run, we finally have 200,000 acceptable values saved for each parameter.

4.2.2. Priors

As reviewed in the introduction section, there are many lensing degeneracies, which can lead to large uncertainties in the measurement of lens mass distributions but leave the lensed images and flux ratios almost invariant. The lensed images can provide only limited information about the lens mass distribution in the annulus encompassing them. In regions without clear lensing features, the estimation of the mass distribution is just an interpolation or extrapolation based on a lens mass model (Kochanek 2020). In other words, when we choose a lens mass model, for example, with only one or two free parameters in the radial direction, rigid priors have already been applied, and the significance of systematics strongly depends on the consistency between the adopted lens model and the true mass distributions.

The BPL profile has more than three degrees of freedom in the radial direction. In principle, it is likely to result in more reasonable constraints on lens mass distributions. However, we find in the next section that, if we do not impose priors on the radial profile of the BPL model, the biases or uncertainties for the mass distributions within Einstein radii could still be significant,

depending on the configuration and signal-to-noise ratio of the extracted lensed images. Therefore, it is essential to add reasonable priors to certain parameters. In this work, we pay special attention to the priors on the central black hole mass m_b , axis ratio q and the inner density profile (r_c and α_c) for the BPL model. These quantities are constrained by using stellar mass (or light) distributions.

Central black holes can have detectable effects on the formation of central images (Mao et al. 2001) and be closely related to the velocity dispersions (Gebhardt et al. 2000). However, due to the lack of central images or the low signal-to-noise ratio of lensed images in the central region, it is usually very hard to determine the mass of central black holes based solely on SL observations. To account for the effect of central black holes, we resort to the relation between central black hole mass m_b and total stellar mass M_* of galaxies (Häring & Rix 2004; Kormendy & Ho 2013; Reines & Volonteri 2015), which is parameterized by

$$\log(m_b/M_\odot) = a + b \log(M_*/10^{11}M_\odot). \quad (20)$$

The left panel of Figure 3 illustrates the fittings to the relation between m_b and M_* of 5343 Illustris galaxies. The solid and dashed lines are for the elliptical and disk galaxies, respectively. For clarity, we only plot the data points for the elliptical galaxies.

Note that the galaxy types are defined according to the Sérsic indices and stellar dynamical properties of galaxies (please refer to the details in Du et al. 2020). We find that, for elliptical galaxies, the best-fit values are

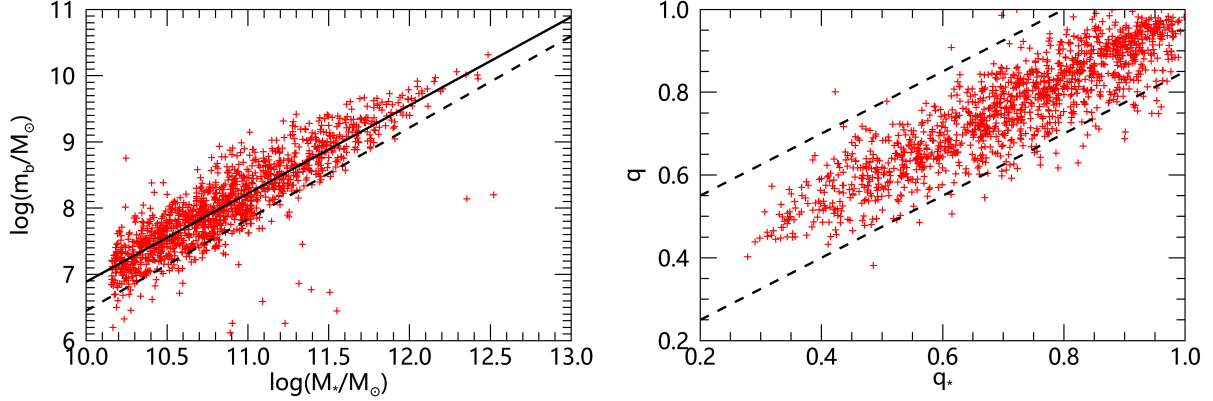


Figure 3. Left: relation between central black hole mass m_b and total stellar mass M_* . The black solid line shows the best-fit to the red pluses corresponding to ~ 1300 elliptical galaxies. For reference, the dotted line shows the best-fit for disk galaxies. Right: comparison between axis ratios of overall mass and stellar mass distributions. The dashed lines indicate the artificially defined upper and lower limits of the axis ratios q for overall mass distributions given the axis ratios q_* for stellar mass distributions.

$a = 8.22$ and $b = 1.33$, comparable with the observations (e.g., Sijacki et al. 2015). For disk galaxies, $a = 7.83$ and $b = 1.38$. The intrinsic scatters around the best-fit lines are about 0.34 and 0.29 dex for elliptical and disk galaxies, respectively. It should be mentioned that, in practical fitting, we do not take into account the scatter of the black hole mass for each galaxy but fix it to be the value at the best-fit relation.

The second non-negligible quantity is the ellipticity which by inspection has evident degeneracy with other lens model parameters, e.g., amplitude b and density profile slopes (see also the Fig.B.1 in Millon et al. 2020, for example). In the right panel of Figure 3, we present the correlation of axis ratios between overall mass and light (i.e., stellar mass) distributions for elliptical galaxies. For disk galaxies, we find a very similar scatter diagram with only a slight shift. These axis ratios are estimated by simultaneously fitting the corresponding surface mass and light distributions in a FoV of $14'' \times 14''$ using the BPL and PL-Sérsic profiles with the same inner density slope and break radius. The two dashed lines show the upper ($q = 0.75q_* + 0.4$) and lower ($q = 0.75q_* + 0.1$) limits of the axis ratios q of overall mass distributions given the axis ratios q_* of stellar mass distributions, which are adopted to confine the ellipticities of lens mass distributions in model fittings.

The third prior is about the inner density profile which is hard to constrain if there are no identifiable lensed images in the inner or central region. In order to make the lens mass modeling more efficient and accurate, we propose constraining the inner part of mass distributions by resorting to light distributions, in view of the fact that baryonic matter dominates the overall mass in the core region of galaxies. For implementing this idea, we prefer using the PL-Sérsic profile to fit the lens light

distributions first. In addition, we assume that the lens mass and light distributions share the same break radius and inner slope.

As we know, at the break radius r_c of the PL-Sérsic profile, the logarithmic slope of the Sérsic part can be written as

$$\alpha_j = -\frac{d \ln j(r)}{d \ln r} \Big|_{r=r_c} = u + \nu \left(\frac{r_c}{s} \right)^\nu. \quad (21)$$

The break radius of the PL-Sérsic profile can thus be expressed by

$$r_c = s [(\alpha_j - u)n]^n. \quad (22)$$

This indicates that, from the point of view of model fitting, we may artificially define a break radius using the Sérsic part of the PL-Sérsic profile, where the logarithmic slope of the Sérsic part is α_j .

So, the aim now is to find a break radius for each lens using the lens light distribution, within which the inner slopes are assumed to be the same between lens mass and light distributions. Based on a series of tests, we find that the break radius $r_{c,2.3}$ defined by $\alpha_j = 2.3$ is a fairly good choice for distinguishing the inner part from the outer part of mock lenses.

Here is a test showing the 3D fittings to the volume density profiles of ~ 5000 Illustris galaxies. Specifically, for each Illustris galaxy, we first fit its 3D light distribution within 90% light radius using the PL-Sérsic profile to get the break radius $r_c = r_{c,2.3}$ and the inner slope $\alpha_c = \alpha_{c,2.3}$. With fixed r_c and α_c given by the light profile fitting, the volume mass density profile is then fitted by the BPL model with the same radii as those used for the light profile fitting. In Figure 4, we present the distributions of slopes (inner and outer slopes) in the left panel and break radii in the right panel for Illustris

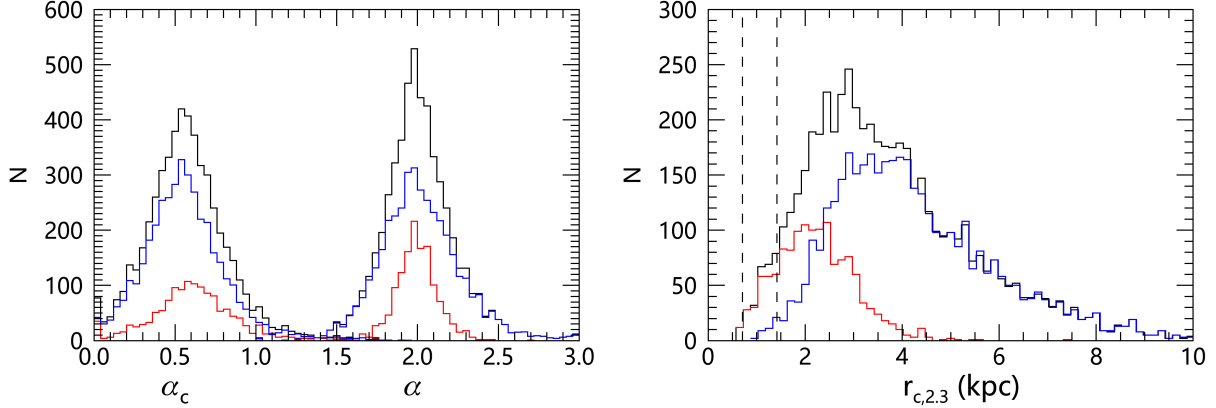


Figure 4. Left panel: distribution of inner slopes α_c and outer slopes α of mass density profiles, where α_c are estimated from PL-Sérsic profile fittings to the 3D light distributions with break radius $r_{c,2,3}$. Right panel: distribution of $r_{c,2,3}$. The two vertical dotted lines in the right panel mark the softening lengths in Illustris simulation for the stellar ($0.5h^{-1}$ kpc) and dark matter particles ($1h^{-1}$ kpc), respectively. In both panels, the red and blue histograms are for the elliptical and disk galaxies, respectively. The black histograms are for all the galaxies.

galaxies. It is found that, with the definition of $r_{c,2,3}$, the inner part of mass distributions can be clearly distinguished from the outer part. It is also demonstrated that the outer slopes α are around 2 and almost independent of galaxy types. The scatters of α are ~ 0.13 for elliptical galaxies and ~ 0.23 for disk galaxies. These results are in agreement with those found by the 2D “joint” fittings with FoV $6'' \times 6''$ shown in Figure 6 of Du et al. (2020).

In addition to the priors mentioned above, for the BPL model, we also examine the necessity of limiting the outer slopes, for example, confining the outer slopes in a range of $\alpha = 1.8$ to 2.2 . For the other parameters in model fittings, uniform priors are applied with sufficiently large ranges.

Note that, in this paper, we single out individual Illustris galaxies for our analyses. Therefore no large-scale structures are included, and consequently negligible effects from external convergence and shear. Even if a shear component exists due to correlated substructures or angular structures, its effect can be mimicked to some extent by ellipticity because of the well-known degeneracy between ellipticity and shear (Kassiola & Kovner 1993; Luhtaru et al. 2021).

Also note that, for SIE and SPL models, we do not account for the central black holes and the above-mentioned limitations on axis ratios. For the BPL model, there are two cases. One is denoted as “BPL-rigid” with the above-mentioned priors for black hole mass (m_b), axis ratio (q), break radius (r_c), inner (α_c) and outer (α) slopes. The other is denoted as “BPL-free” for comparisons, which retains the prior on the axis ratio, but does not have strong priors on the black hole mass, break radius and slopes. Table 1 shows the spe-

Table 1. Priors on the radial parameters.

Model	α	α_c	r_c	m_b
SIE	2	0	0	0
SPL	$1.2 \sim 2.8$	0	0	0
BPL-free	$1.2 \sim 2.8$	$0 \sim 2.8$	$0 \sim 1''.5$	$0 \sim 10m_b^*$
BPL-rigid	$1.8 \sim 2.2$	$\alpha_{c,2,3}$	$r_{c,2,3}$	m_b^*

NOTE—The parameter b , which is not listed above, is set to be $0''.1 \sim 3''.5$ for all the models. The symbol m_b^* denotes the black hole mass inferred from the total stellar mass of a lens galaxy.

cific priors on the radial parameters of the BPL model, where the SIE and SPL models are two of the special cases. It is noticeable that there are two degrees of freedom in the radial direction for BPL-rigid and SPL models, while one for SIE and five for BPL-free models.

With the addition of axis ratios, position angles and two position parameters for a center, there are in total seven free parameters for a background source, and five, six, nine and six free parameters for the SIE, SPL, BPL-free and BPL-rigid lens mass models, respectively. We find that, for the SIE and SPL models, the MCMC fitting usually takes ~ 8 CPU hours to reconstruct a SL image, while it takes about 24 and 20 CPU hours for the BPL-free and BPL-rigid models, respectively.

5. RESULTS

In this section, we investigate the performance of the BPL model as well as its special cases (*e.g.*, the SIE and SPL models) in reconstructing the lensed images, lens

mass and source light distributions. We also examine the accuracy of estimating AL-weighted LOSVDs.

5.1. Lensed image and lens mass reconstructions

5.1.1. Individual examples

As an example, Figure 5 shows the reconstruction of lensed images and radial convergence profiles of three mock SL systems with single exposure. It is noticed that, the SIE and SPL models can reproduce the lensed images around Einstein radius quite well, but cannot recover the lensing features toward the center and the inner density profiles accurately. The BPL-free model, which is more flexible in the radial direction, succeeds in recovering the lensed images and radial convergence profiles of the lens 152864 (the number here is the subhalo id in the Illustris-1 simulation), but fails for the other two lenses.

We show the results of BPL-rigid model fittings in the fifth column of Figure 5. It is amazing that, for all the three SL systems, the lensed images and radial convergence profiles can be recovered with high fidelity, although the relevant χ^2 values may not be the smallest. These results illustrate the necessity of adding priors to the radial density profiles, especially in the inner region where the central images, if they exist, may be too faint to be detected due to the significant contamination of lens light distributions. The BPL model has the ability to find out the possible central images by using the lens light distributions to constrain the inner density profiles.

We know that the image quality can be improved by multiple exposures. However, by inspecting the lensed images extracted from the SL images with four exposures, we find the contamination from lens light cannot be effectively reduced by increasing exposure time for galaxy-scale lenses. The extracted lensing features for multiple exposures are almost the same as those for single exposure, and so are the reconstructed lensed images and convergence profiles, although the lensing images with more exposures suffer less from the cosmic rays and poisson noise.

An ideal case is that the foreground lens light is perfectly subtracted from SL images. We investigate this case based on the mock SL images with four exposures (2200s in total). Similar to Figure 5, Figure 6 shows the relevant results, where the first column displays the lensed images left after subtracting the true lens light directly. Compared to Figure 5, the extracted lensed images become more clear, although there are still poisson noises from lens light.

Figure 6 shows that, even if there are no lens light contaminations, it is impossible for SIE and SPL models to recover the lensed images and convergence profiles in

the central region. The BPL-free model can now reconstruct well the lensed images and convergence profiles of the lens 132701, but still fails for the lens 1 whose central image disappears in noise. When looking at the accuracy of mass measurements rather than χ^2 values for image reconstructions, the BPL-rigid model with strong radial priors still performs best.

Both in Figure 5 and 6, the blue (red) shaded bands show the $\pm 3\sigma$ error ranges of the reconstructed radial (mean) convergence profiles. It is demonstrated that, compared to their deviations from true profiles, the uncertainties estimated from model fittings are subdominant in most cases. We thus do not pay attention to the precision or statistical errors of the relevant quantities for each lens system, but focus on the statistics about the best-fit values or reconstructions.

5.1.2. Einstein radii

For an elliptical lens, its Einstein radius inferred from a model fitting is defined as the elliptical radius $R_{E,el}$ within which the mean convergence satisfies $\bar{\kappa} = 1$. This definition of elliptical Einstein radius avoids the azimuthal integral in evaluating the circular Einstein radius. For a smooth elliptical mass model, a little bias may exist between elliptical and circular Einstein radii, but it is negligible in practice, as shown in Figure 7, because of the complexity of true mass distributions, *e.g.*, angular structures and variation of ellipticities with radius.

Figure 7 shows the comparisons of the best-fit Einstein radii $R_{E,el}$ and the directly measured Einstein radii R_E defined by a circle, for different model fittings and noise levels. It is shown that, independent of lens models and noise levels, the Einstein radius can always be estimated with negligible bias (typically subpercent). However, the uncertainties in R_E estimation are model dependent.

It is shown that, in each panel, the red histograms for the multiple exposures are very similar to the black histograms for the single exposure. Their scatters are almost the same, indicating the limitation of using more exposures to get a better inference of Einstein radius. This is mainly because the light contamination from main lens itself cannot be effectively reduced by more exposures. If we artificially subtract the true lens light, as shown by the blue histograms and its 68% central confidence interval, the accuracy in R_E estimation can be largely improved to $2 \sim 5\%$, depending on the adopted lens mass models.

Also focusing on the black and red histograms, we find the scatters for SIE, SPL and BPL-free models are typically greater than 5% and can even reach up to $\sim 9\%$. For the BPL-rigid model with inner density profile

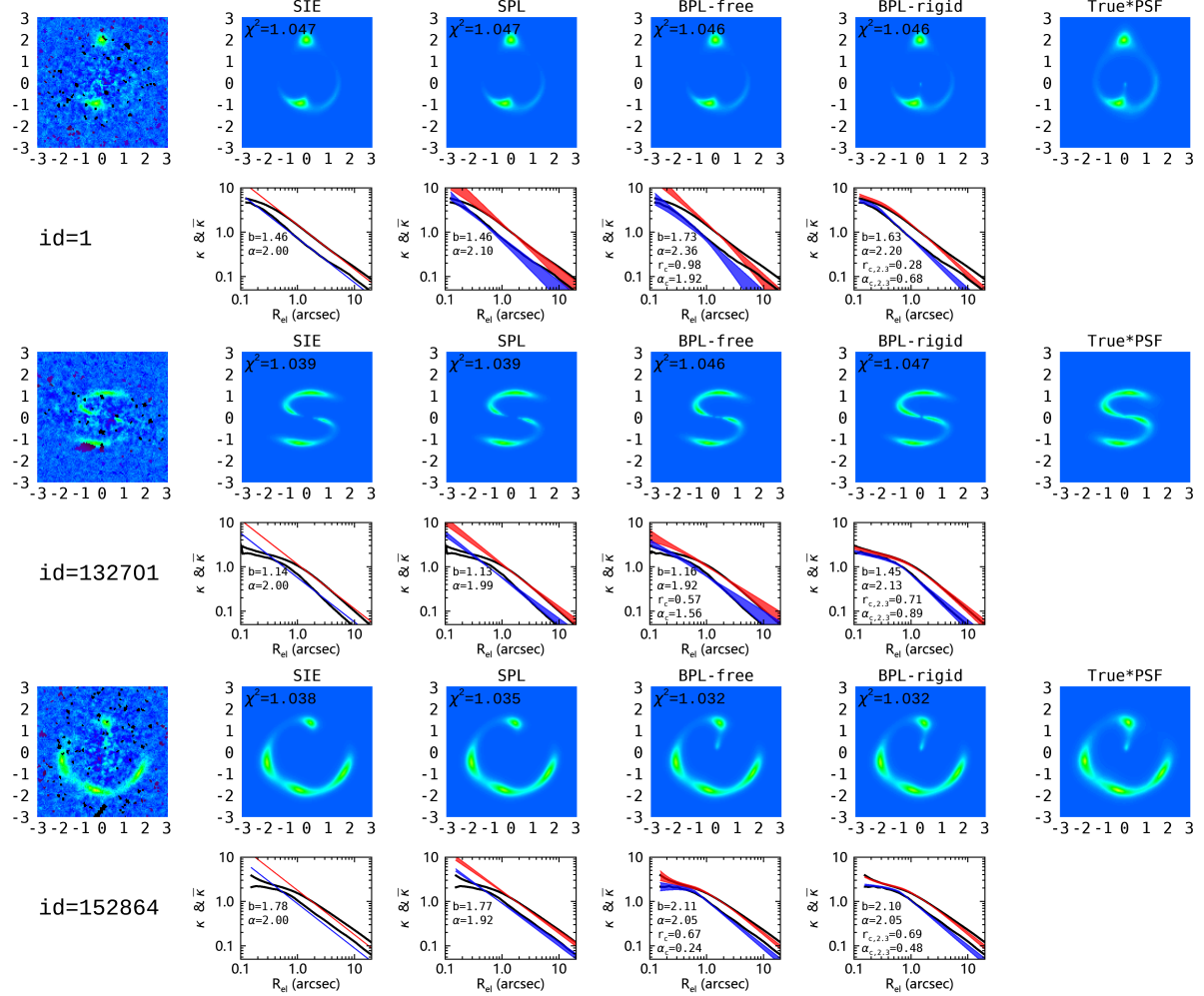


Figure 5. Lensed image and lens mass reconstructions for three single-exposure mock SL systems with $id = 1$ (top two rows), 132701 (middle two rows) and 152864 (bottom two rows). The leftmost and rightmost columns present the extracted and true lensed images in a FoV of $6'' \times 6''$, respectively. The middle four columns from left to right display the reconstructed images (odd rows), along with the corresponding reconstructed convergence profiles (even rows), based on SIE, SPL, BPL-free and BPL-rigid models, respectively. The reduced χ^2 values for the reconstructed images are shown at the left-top corner of the corresponding panels. In the panels about convergence profiles, the true radial convergence (κ) and mean convergence ($\bar{\kappa}$) profiles are shown by black lines, where $\kappa(R_{\text{el}}) < \bar{\kappa}(R_{\text{el}})$ and R_{el} is the elliptical radius. The blue and red shaded bands indicate the $\pm 3\sigma$ error bands around the best-fit values. Also shown are the best-fit values relevant to the radial profiles.

predetermined, the fractional uncertainty in estimated Einstein radius can be smaller than 5%. In any case, we find the fractional uncertainty in R_E estimation is unlikely to be better than 2% even for the idealized case without lens light contamination.

5.1.3. Radial convergence profiles

We now inspect the accuracy of reconstructed radial convergence profiles over a wide range of radii from $0.1R_E$ to $10R_E$. Figure 8 shows the statistical results of mean convergence profiles as a function of elliptical radius. It is noticeable that, close to Einstein radius, both biases and scatters approach the minimum regardless of lens mass models or noise levels. Away from Einstein

radius, the scatters tend to be larger and larger, indicating the difficulty in recovering the mass distributions in these regions.

It is also evident that the biases and scatters for SIE and SPL models are rather large within Einstein radius, which can be greatly reduced by using the more flexible BPL model. Especially for the BPL model with rigid priors, the biases are typically less than 5% within R_E , and less than 2% at R_E . For the BPL-free model, it works well within R_E only when the lens light distributions are perfectly subtracted.

Outside Einstein radius, an amazing result is that, the biases for the SIE model are typically less than 10% and the scatters are also not too significant. The SPL model

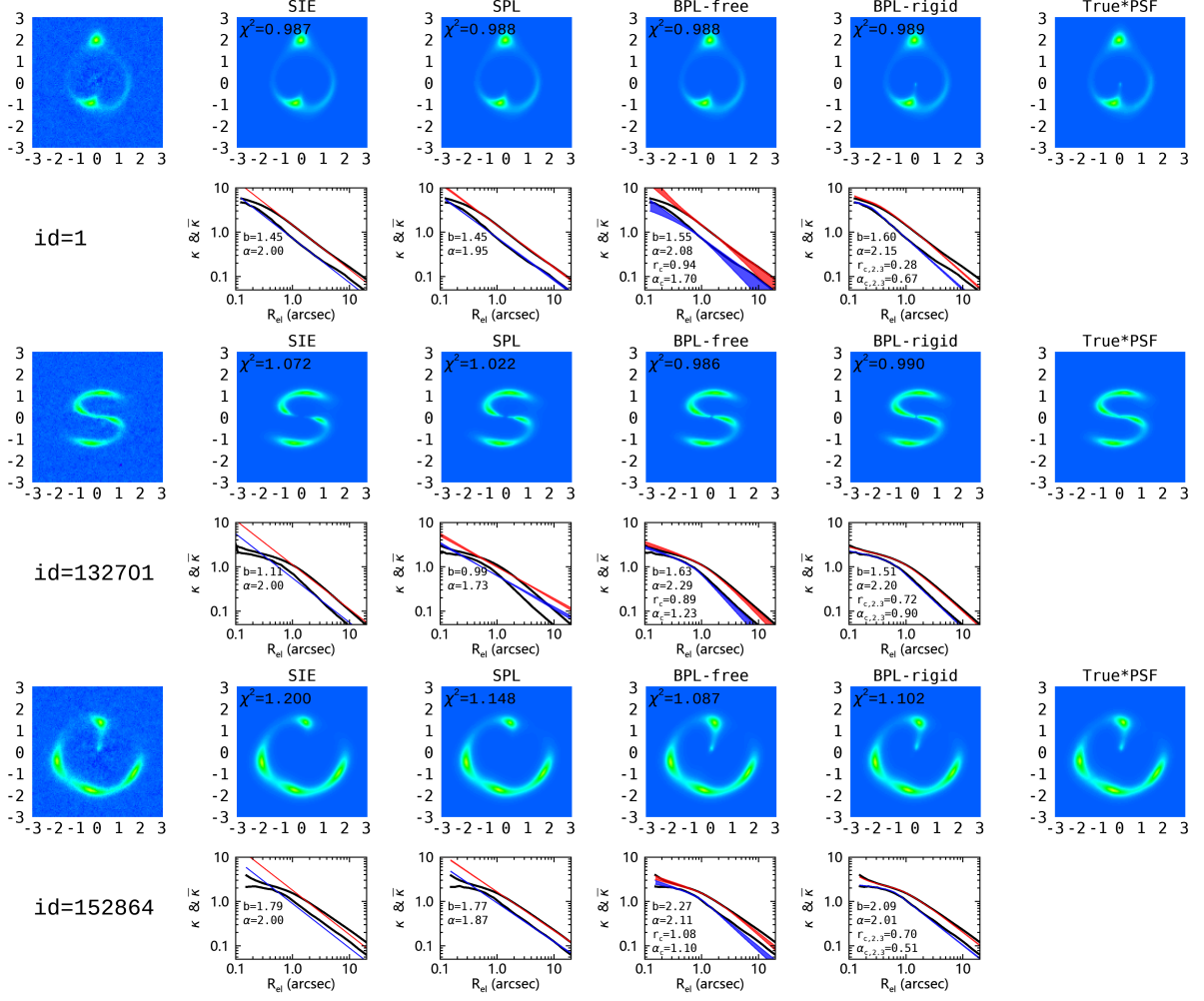


Figure 6. Similar to Figure 5 but for multiple exposures with perfect subtraction of foreground lens light distributions.

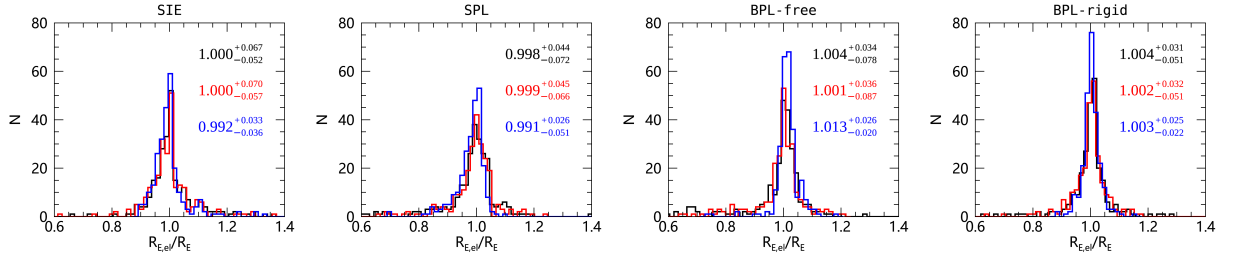


Figure 7. Distributions of the ratios between best-fit elliptical Einstein radii $R_{E,el}$ and their true values R_E . In each panel, the black, red and blue histograms are for the cases with single exposure, four exposures and four exposures with perfect subtraction of lens light, respectively. For each histogram, also shown is its median value along with the 68% confidence interval.

still produces large scatters away from Einstein radius. It is shown that the BPL-free model is not good at constraining the convergence profiles at radii larger than R_E . By adding strong priors to the radial parameters, the BPL-rigid model can recover the mean convergence profiles within $3R_E$ quite well, with biases less than 5% and controllable scatters.

It is worth noting that the large biases and scatters within R_E for SIE and SPL models may not be true for real galaxy lenses, which lack large and flat cores. Nonetheless, the first two columns of Figure 8 demonstrate the failure of the SIE and SPL models to reconstruct the more flexible lens mass distributions.

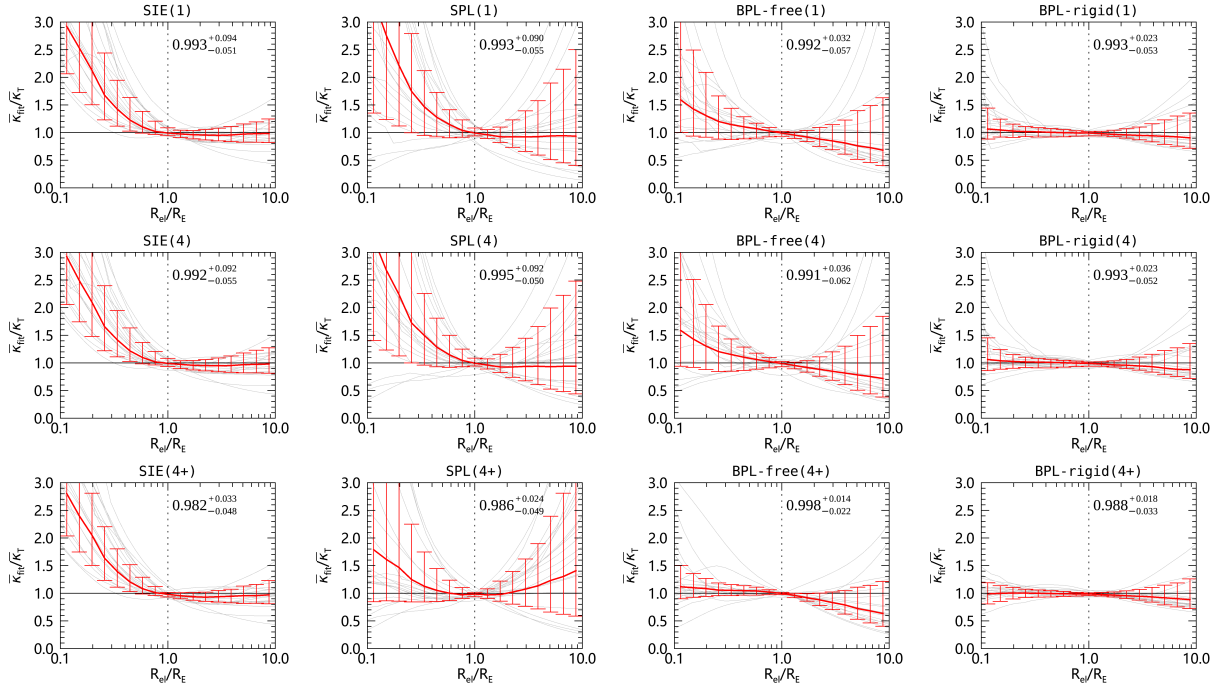


Figure 8. Comparison of reconstructed mean convergence profiles $\bar{\kappa}_{\text{fit}}$ and true ones $\bar{\kappa}_T$ as a function of elliptical radius R_{el} scaled by true Einstein radius R_E . The lens mass models used for image reconstructions are indicated by the titles, with (1), (4) and (4+) signifying the single exposure, four exposures and four exposures with perfect subtraction of lens light, respectively. We show 20 gray lines in each panel which correspond to 20 randomly selected SL systems. The red lines show the median trend of $\bar{\kappa}_{\text{fit}}/\bar{\kappa}_T$ for the 257 grade-A lenses. The error bars show the 68% central confidence intervals at the corresponding radii. The vertical dotted line in each panel marks the Einstein radii, at which the median and $1-\sigma$ error of $\bar{\kappa}_{\text{fit}}/\bar{\kappa}_T$ are presented.

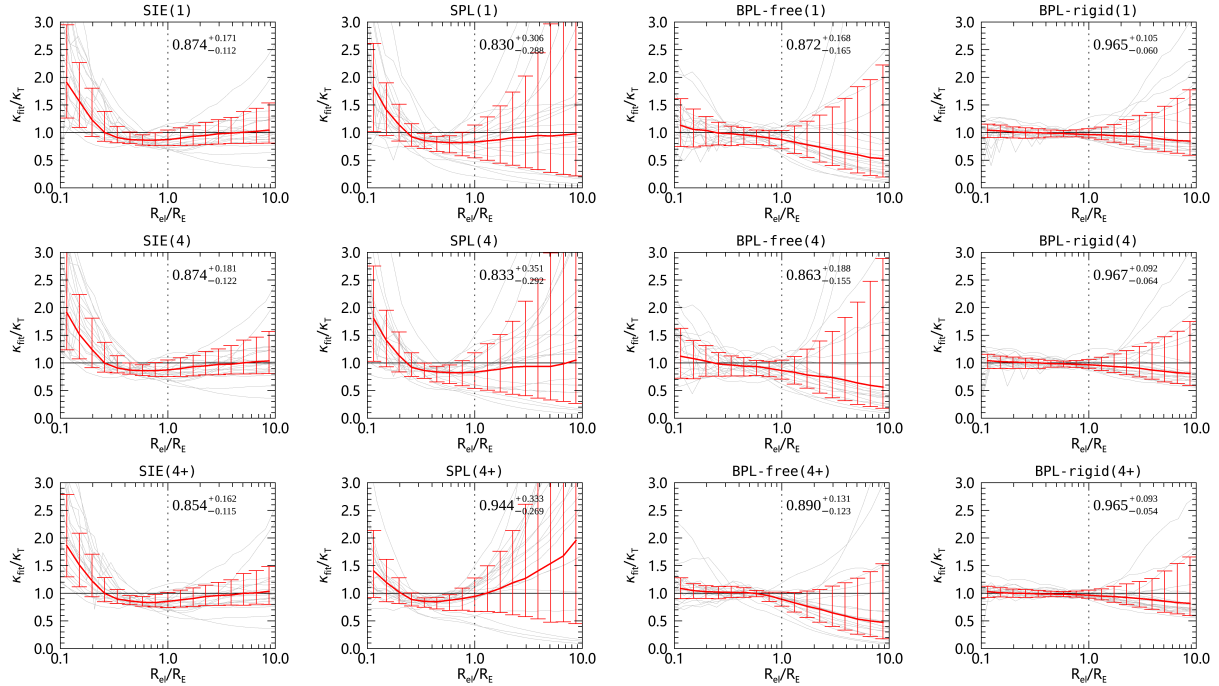


Figure 9. Similar to Figure 8, but for the radial convergence profiles $\kappa(R_{\text{el}})$.

In addition to the mean convergence profiles, we are also interested in the radial convergence profiles, especially the convergence κ_E at Einstein radius. In Figure 9, we exhibit the deviations of the reconstructed convergence profiles from the true profiles. We realize again that, without reasonable priors or additional information on the mass distributions, it is impossible to constrain the radial convergence profiles over a wide range of radii based solely on lensed images. As shown in the last column of Figure 9, the BPL-rigid model outperforms all the other models. Within R_E and $3R_E$, the biases are typically no more than 5% and 10%, respectively.

Figure 9 also shows that the scatters in κ_E measurements are quite large, especially for the SPL model fittings. Large uncertainties in κ_E make difficult the accurate measurements of H_0 from time delay cosmography, because of the well-known scaling relation $H_0 \propto 1 - \kappa_E$ (Kochanek 2020, 2021). The fractional error in H_0 can be roughly evaluated by $f_{H_0} = (1 - \kappa_{E,\text{fit}})/(1 - \kappa_{E,\text{T}}) - 1$, where $\kappa_{E,\text{fit}}$ and $\kappa_{E,\text{T}}$ are the fitted and true convergences at R_E , respectively. By calculating f_{H_0} , we find its median reaches $\sim 20\%$ for SIE, SPL and BPL-free models, let alone the much larger scatters. For the BPL-rigid model, the bias in H_0 is less than 6%. Taking also scatters into consideration, we conclude that, even for the BPL-rigid model, H_0 can probably only be constrained to an accuracy of $\sim 10\%$ for a single SL time-delay system.

5.2. Background source light reconstructions

We in Figure 10 show the source light reconstructions for the three SL systems with id = 1, 132701 and 152864, whose mass reconstructions are shown in Figure 5 and 6 as examples. The top panels display the source light properties estimated in the case of single exposure, while the bottom panels are for the multiple exposures with perfect removal of lens light. By looking at the ellipses, it is noticed that the centers, ellipticities and position angles of the reconstructed source light distributions are highly correlated between different lens mass models, although large offsets may exist compared to the true values. Statistically, we find that the correlation coefficients for centers, ellipticities, and position angles predicted by different lens mass models are all greater than 0.8. There are also weak correlations for parameters I_0 and n between different lens model fittings to the same lensed images, as shown by the parameter values listed in each panel.

By comparing the corresponding ellipses in the bottom panels to those in the top panels, we realize that the improvement in image quality cannot effectively reduce

the center offsets of source galaxies. However, if there is no visible contamination from lens light, the amplitude I_0 and Sérsic index n become more consistent with the input values.

Figure 11 exhibits the statistical distributions of the differences between estimated and input source parameter values. The black histograms are for the single-exposure cases, while the red are for multiple-exposures without lens light contamination. We do not plot the histograms for multiple-exposures with significant lens light contamination, which are very similar to the histograms for single-exposure cases. It is now more clear that, although there are significant uncertainties, there are no systematic biases for the centers, position angles and ellipticities of the source galaxies.

For single-exposure cases, negative biases exist for central light intensity I_0 and Sérsic index n , demonstrating the significant effect of lens light contamination on the determination of source light density profiles. These biases in I_0 and n disappear when the lens light are perfectly modeled and subtracted.

Of the measurements of source parameters, the most complicated one is the inference of effective radius which is not only sensitive to lens light contamination but also lens mass models. The lens light contamination may spoil the lensed images, while the lens mass models may introduce bias in mass distributions around Einstein radius and thus the magnifications. It is shown that, for single-exposure cases, the SIE, SPL and BPL-free models coincidentally give unbiased estimates of effective radii. However, for the cases without lens light contamination, the effective radii for SIE and BPL-free models tend to be larger, as indicated by the red histograms in the fourth column of Figure 11. The bias in R_{eff} for the SPL model remains almost unchanged since the reconstructed mass distributions for the SPL model instead have smaller biases around Einstein radii. By contrast, when there is no lens light contamination, the BPL-rigid model can provide a more reliable and accurate estimate of R_{eff} as well as other source galaxy parameters.

We now pay attention to the large uncertainty in source center determinations. As indicated by Figures 10 and 11, there are cases with large displacements of source centers. For example, the id = 1 with single exposure shows a source center displacement of $\sim 0''.41$. We look for the cause of large offsets of source centers by comparing the true and reconstructed lens mass distributions out to the outskirts of lens halos, and also the deflection fields. As expected, we find that many lenses show complexity of mass distributions in the inner or outer regions, which may induce additional deflections

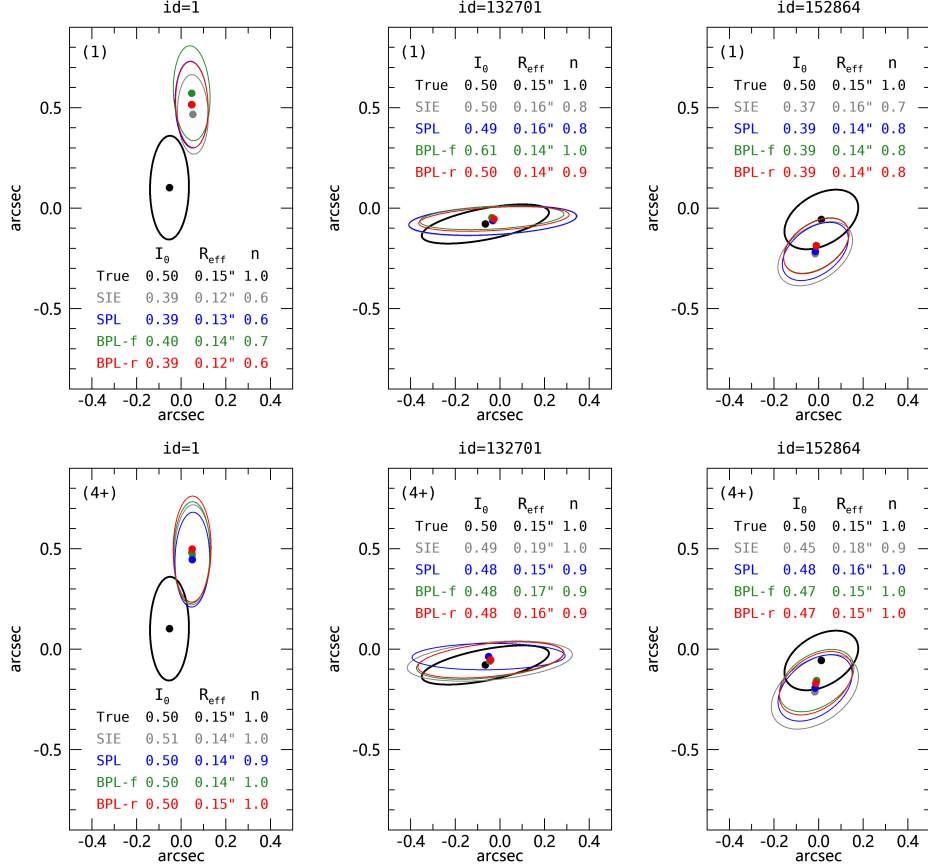


Figure 10. Source light reconstructions for three SL systems from left to right with id = 1, 132701 and 152864, respectively. Top panels show the results for single exposure, while bottom panels for multiple exposures without lens light contamination. In each panel, the ellipses show the isophotes at effective radii of the corresponding source light distributions (black for the true and colored for the reconstructed), and the dots mark their centers. Also displayed are the Sérsic profile values of I_0 , R_{eff} and n corresponding to the ellipses.

around Einstein radii compared to the estimated elliptical mass distributions.

In this paper, we define the additional deflections as the difference between the true and reconstructed deflections. It is noticed that the additional deflections in the central region of a lens can be approximated by a constant vector $(\Delta\alpha_{x,0}, \Delta\alpha_{y,0})$ which is the average of the additional deflections within the Einstein radius. Figure 12 shows the strong correlation between $(\Delta\alpha_{x,0}, \Delta\alpha_{y,0})$ and $(\Delta x_{\text{cen}}, \Delta y_{\text{cen}})$ for the BPL-rigid modeling on lensed images without lens light contamination. It is demonstrated that the center offsets of source galaxies can be largely explained by the existence of constant deflection angles around the centers of lenses. For the case with id = 1, we find the amplitude of its additional constant deflection is $\sim 0''.38$, in line with its source center offset.

5.3. AL-weighted LOSVDs

AL-weighted LOSVDs, denoted as $\sigma_{\parallel} = \langle \sigma_{\parallel}^2 \rangle^{\frac{1}{2}}$ hereafter, can provide complementary constraints on the lens mass distributions, and may help us break MSD. However, in order to implement this idea, we need to ensure there is no bias from modeling itself. For the BPL model, it has been found that velocity dispersion bias exists for direct fittings to surface mass distributions (Du et al. 2020). This velocity dispersion bias can be systematically corrected by $b_{\sigma} \simeq 1.015q_{\star}^{-0.07}$ with q_{\star} being the axis ratio of the lens light distribution.

We in this subsection look at the consistency between predicted and true AL-weighted LOSVDs, where the former is evaluated based on the reconstructed lens mass and directly-fitted lens light density profiles. For SIE and SPL lens mass models, the Sérsic profile is adopted for lens light fittings, whereas for BPL models, the PL-Sérsic profile is adopted. More specifically, for BPL-free modeling, the inner density profiles of lens light distributions are determined by lens mass reconstructions. However, for BPL-rigid modeling, the inner slopes and break

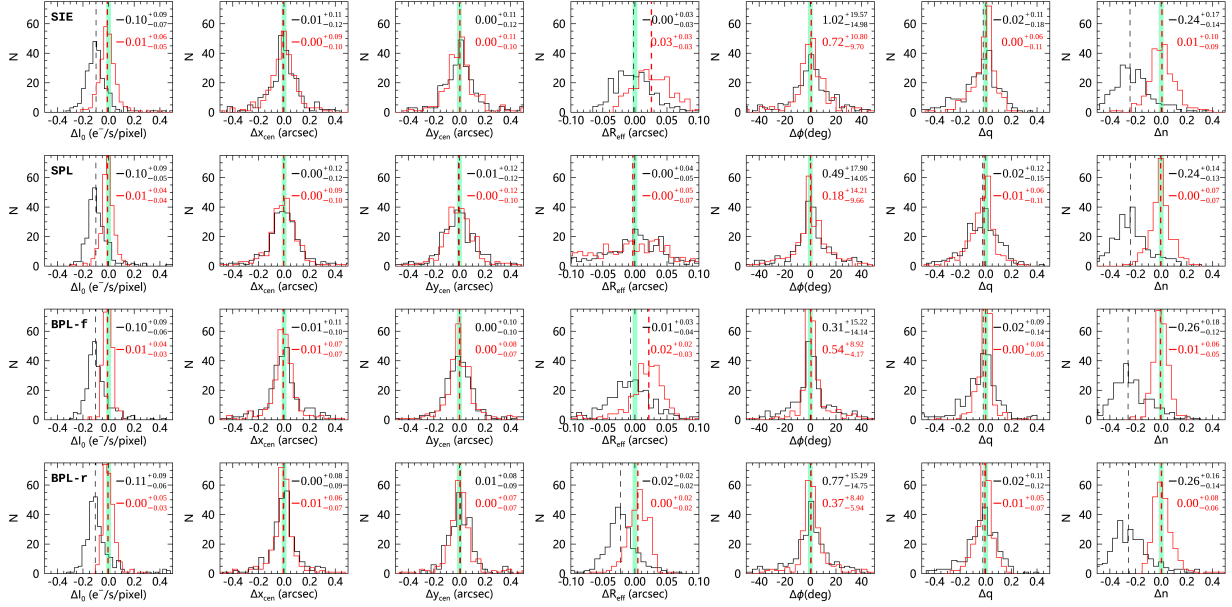


Figure 11. Histograms of the differences between estimated and true Sérsic profile parameter values for the source light distributions. From top to bottom, the panels are for SIE, SPL, BPL-free and BPL-rigid models, respectively. From left to right, the relevant parameters are, respectively, the central light intensity I_0 , source center $(x_{\text{cen}}, y_{\text{cen}})$, effective radius R_{eff} , position angle ϕ , axis ratio q and Sérsic index n . The black histograms represent the cases for single exposure, while the red are for multiple exposures without lens light contamination. Numbers in each panel denote the medians along with central 68% confidence intervals of the corresponding histograms, where the medians are marked by vertical dashed lines. The vertical green bands indicate the positions of zero-deviation. Note that the true values for I_0 , R_{eff} and n are $0.5 \text{ e}^-/\text{s/pixel}$, $0.^{\circ}15$ and 1.0, respectively.

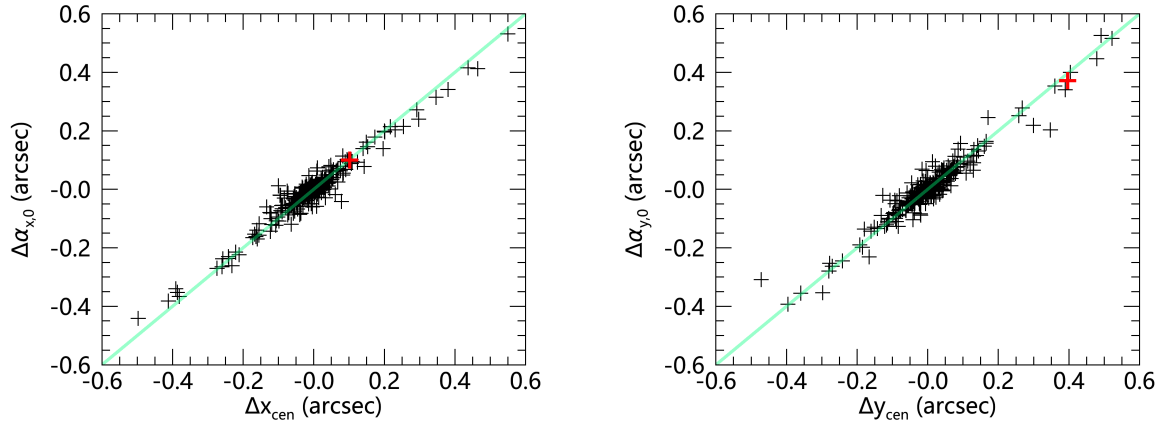


Figure 12. Comparisons between the estimated constant deflections $(\Delta\alpha_{x,0}, \Delta\alpha_{y,0})$ and source center offsets $(\Delta x_{\text{cen}}, \Delta y_{\text{cen}})$ for the BPL-rigid modeling on lensed images without lens light contamination. The left and right panels are for the x - and y -directions, respectively. The red pluses denote the case with id = 1.

radii of lens mass distributions are fixed to be $\alpha_{c,2,3}$ and $r_{c,2,3}$, respectively, which are given by fittings to lens light distributions. Also note that, in the estimation of AL-weighted LOSVD for each lens, the global velocity anisotropy is adopted and assumed to be known.

Figure 13 displays the comparisons of the predicted and true AL-weighted LOSVDs, where the top two rows

correspond to the single exposure cases and the bottom two rows are for the four exposures with perfect subtraction of lens light. We do not present the results for multiple exposure cases with lens light contamination, which are very similar to those for single exposure cases. We can see from the black histograms or the black scatter diagrams that there are positive biases in σ_{\parallel} es-

timations for all the lens mass models investigated in this paper. The biases are typically larger than 5% and have a certain dependence on the lens mass models. We find the uncertainties in σ_{\parallel} estimations are more vulnerable to lens mass models. For instance, the uncertainty for the SPL model can reach up to 30% while it is only about 5% for the BPL-rigid model.

It is also found that the improvement on the lensed image quality has little effect on the systematic biases in σ_{\parallel} predictions but may reduce the uncertainties significantly for some lens mass models. For example, the fractional uncertainty for the BPL-free model can be reduced from 14% to 8%. In contrast, we notice that both the uncertainties and biases for the BPL-rigid model are quite stable, basically insensitive to lens light contaminations. After correcting for the projection effect in the BPL-rigid model fittings, *i.e.*, dividing the predicted σ_{\parallel} by b_{σ} for each lens, the finally obtained σ_{\parallel} can match its true value to within 6%. It is well known that, by comparing the true and predicted velocity dispersions, an effective external convergence can be estimated according to $\kappa_{\text{ext}} = 1 - \sigma_{\parallel, \text{true}}^2 / \sigma_{\parallel, \text{pred}}^2$. We thus expect that, for a SL system, it is possible to infer its external convergence to within 12% accuracy using the BPL-rigid model.

6. CONCLUSION AND DISCUSSIONS

The BPL model proposed by [Du et al. \(2020\)](#) is a lens mass model with four free parameters in the radial direction. In this paper, we examine the performance of the BPL model on the lens mass and source light reconstructions, as well as the predictions of AL-weighted LOSVDs.

In order to quantify the uncertainties in the relevant quantities, an end-to-end test is done by starting with the creation of mock SL observations with various noises, *e.g.*, sky background, cosmic rays, PSF and readout noise. About 100 SLACS lenses are adopted as references for calibrating noise levels and lens statistics. We find a scaling relation between the total number of photon-excited electrons N_e and the total stellar mass M_{\star} of SLACS lenses in HST F814W photometry, which is used to help us transform the stellar mass of Illustris galaxies into lens light distributions in a simple way. The background sources are assumed to be at redshift $z_s = 0.6$ with an apparent magnitude of ~ 23.5 , following a Sérsic profile with an effective radius of $0''.15$ and Sérsic index $n = 1$. We assume that there are two different exposure times (420 s for single exposure and 2200 s for four exposures) for each SL system.

Given the mock SL observations, we first pay attention to the extraction of lensed images, where the B-

spline technique is used to fit the lens light distributions by masking the identifiable lensing features. For the B-spline technique, a fitting strategy with two or three steps is investigated, with the first step fitting to the monopole term of lens light distributions and the second step fitting to the even multipoles with $m = [2, 4, 6, 8]$. The third step fitting to the odd multipoles will be run only if there are obvious odd features. We finally have ~ 260 “grade-A” lenses left with both single and multiple exposures for further analyses.

We employ forward modeling to reproduce the lensed images, along with lens mass and source light distributions. Four lens mass models are investigated, which are in fact the special cases of the BPL model. They are the SIE, SPL, BPL-free and BPL-rigid models. The SIE model has a slope of 2, while the SPL model has a single free slope. The difference between BPL-free and BPL-rigid models is whether or not strong priors are applied to the radial profiles of the BPL model.

We use ~ 5000 Illustris galaxies to evaluate the relations between overall mass and stellar mass (or light) density profiles, which are adopted as priors to shrink the parameter space in lens mass model fittings. The scaling relations between black hole mass and stellar mass are derived for elliptical and disk galaxies, respectively. We find the axis ratios of surface mass distributions can be confined to a limited range by the axis ratios of surface light distributions. Because baryons dominate the mass in the central region of galaxies, we assume there exists a break radius within which the overall mass and light distributions have the same inner density slopes. We find that this break radius can be well approximated by a radius $r_{c,2.3}$ at which the logarithmic slope of the 3D light distribution is ~ 2.3 . In practice, we evaluate $r_{c,2.3}$ and $\alpha_{c,2.3}$ by fitting the 2D light distributions with the PL-Sérsic profile.

Additionally, we also inspect the model fittings to the four exposure cases with lens light perfectly subtracted. In total, we have three noise levels (*i.e.*, the single and four exposures with lens light distributions fitted by the B-spline technique, and the four exposures with perfect subtraction of lens light) with four lens mass models (*i.e.*, SIE, SPL, BPL-free and BPL-rigid) for each “grade-A” system.

By looking at the lensed image reconstructions, we find that, if there are no obvious central images identified, the extracted lensing features around Einstein radii can always be recovered fairly well, almost independently of lens mass models. Based solely on the χ^2 values of the image fittings, it is hard to judge which lens mass model performs best in reconstructing the lens mass distributions. If central images are evident in the

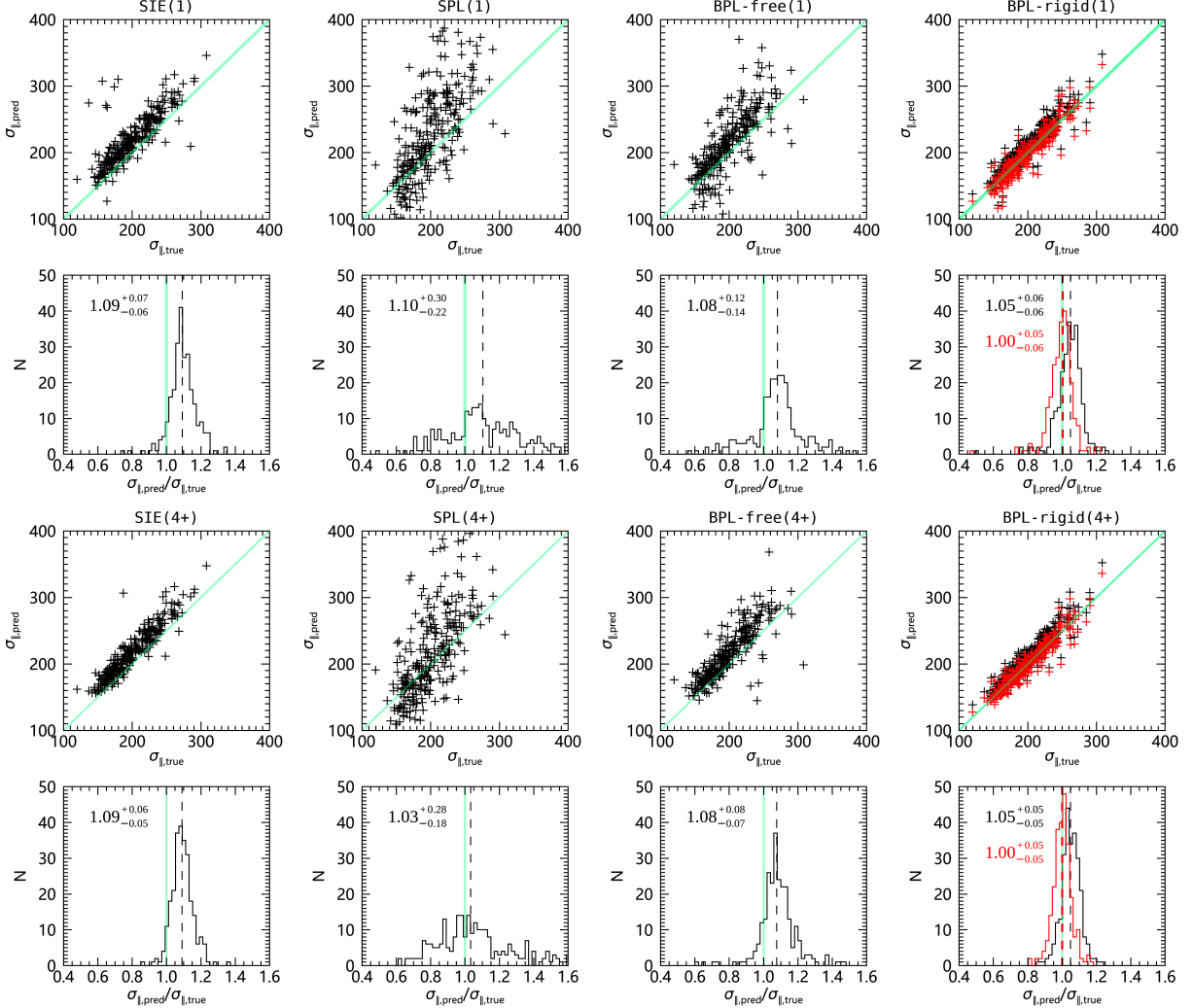


Figure 13. Comparisons of the predicted AL-weighted LOSVDs $\sigma_{\parallel,\text{pred}}$ to their true values $\sigma_{\parallel,\text{true}}$. From left to right, the columns correspond to SIE, SPL, BPL-free and BPL-rigid models, respectively. The top two rows show the results for the single exposure cases, while the bottom two rows are for the multiple exposures without lens light contamination. The scatter diagrams present the one-to-one comparisons, with green lines indicating the identity lines. The histograms show the corresponding distributions of ratio $\sigma_{\parallel,\text{pred}}/\sigma_{\parallel,\text{true}}$, where vertical dashed lines show the medians of the distributions and green lines mark the position without bias. The numbers represent the medians along with 68% confidence intervals. In the rightmost panels, the red pluses and histograms correspond to the results by accounting for the velocity dispersion bias b_σ for BPL models.

extracted lensed images, the BPL models outperform the singular power-law models in both lensed image and lens mass reconstructions. On the other hand, if central images are submerged in lens light, the BPL-rigid model is capable of finding out the missing central images.

We investigate the accuracy of Einstein radius measurements by comparing the elliptical Einstein radii $R_{\text{E,el}}$ inferred from model fittings with the “true” circular Einstein radii R_{E} . Although different definitions of Einstein radius may lead to some inconsistency, we find that the inferred Einstein radius $R_{\text{E,el}}$ is a fairly good estimate of R_{E} . It is shown that the Einstein radius can be measured with negligible bias, regardless of lens mass

models or noise levels which however have large effects on the uncertainties in R_{E} estimation. The BPL-rigid model, which is found to be more accurate than the SIE, SPL and BPL-free models, can determine the Einstein radius to an accuracy of 5% or better, depending on the quality of extracted lensed images.

An accurate measurement of the Einstein radius implies an accurate measurement of the enclosed mass within it. This is indeed the case, as shown in Figure 8. It is shown that all the lens mass models investigated in this paper can measure the radial mean convergence around Einstein radius with negligible biases and controllable uncertainties. However, away from Einstein ra-

dius, the mean convergence profiles are hard to constrain unless rigid priors are added to restrict the BPL model. We demonstrate that the BPL-rigid model can recover the mean convergence profiles quite well, with biases less than $\sim 5\%$ within $3R_E$ and less than $\sim 10\%$ within $10R_E$.

As for the radial convergence profiles, we find the biases at Einstein radius for the SIE, SPL and BPL-free models are typically larger than 10%, along with much larger uncertainties. For the BPL-rigid model, the bias of the convergence at Einstein radius is typically less than 4% with $\sim 10\%$ scatters. It is difficult to constrain the radial convergence profiles over a broad range of radii based solely on lensed images. Among the lens mass models investigated, we find that the BPL-rigid model is the most successful one in recovering the radial convergence profiles, with biases typically no more than 5% and 10% within R_E and $3R_E$, respectively.

We also inspect the source light reconstructions in detail. It is demonstrated that, despite significant uncertainties, there are basically no systematic biases in the estimation of centers, position angles and axis ratios of the source galaxies. We find that lens light contamination can significantly bias the estimation of the radial profile of source light distributions, *e.g.*, the central light intensity I_0 , effective radius R_{eff} and Sérsic index n . The biases in I_0 and n can disappear when the lens light contaminations are insignificant. However, the inference of R_{eff} is also sensitive to lens mass models in addition to the lens light contaminations. We realize that, to a large extent, the center offsets of source galaxies can be attributed to the existence of constant deflection angles in the central region of lenses, which are mainly caused by the complexity of lens mass distributions, *e.g.*, deviations from smoothness and elliptical symmetry.

We look into the consistency between predicted and true AL-weighted LOSVDs. It is found that there exist positive biases ($\geq 5\%$) in the estimation of AL-weighted LOSVDs, and this positive bias cannot be reduced by improving the quality of lensed images. For the BPL-rigid model, we notice that the positive bias can be effectively eliminated by accounting for the projection effect, leading to an uncertainty of no more than 6% in the prediction of AL-weighted LOSVDs. We thus conclude that, with the BPL-rigid model, it may be feasible to evaluate the external convergence to within 12% accuracy for a SL system by comparing its true AL-weighted LOSVD with that predicted from the reconstructed lens mass distribution.

In short, we notice that a good fit to the lensed images does not necessarily indicate a good measurement of the lens mass or source light distributions. With suit-

able priors, the BPL model can significantly outperform the singular power-law models in the reconstruction of lensed images and lens mass distributions, as well as the prediction of AL-weighted LOSVDs. In any case, we find that the Einstein radius cannot be constrained to be more accurate than 2% statistically by the smooth lens mass models investigated in this paper. Because of the large uncertainty of convergence measurement at Einstein radius, the fractional error in H_0 is unlikely to be much smaller than 10% for a single SL time-delay system.

Finally, there are some issues to mention. One is about the mock lenses that are picked out from Illustris galaxies. As we know, the Illustris galaxies have large flat cores due to the softening effect, and are much larger than observed galaxies (Bottrell et al. 2017; Xu et al. 2017). The existence of flat cores largely increases the probability of forming central images and makes larger the deviations of mass distributions from the SIE and SPL models in the central region. So some relevant uncertainties reported in this paper for the SIE and SPL models may be overestimated.

Because the mock lenses are too large, lens light contamination may be too significant in our mock SL images. As shown in Fig 7, there are a few outliers whose Einstein radii are remarkably underestimated or overestimated. We find that most of them exhibit inconsistent lensing features with the true ones, demonstrating the significant effect of lens light contamination or the failure of the B-spline technique in extracting the lensed images of these cases. This also indicates that the criteria for defining “grade-A” lenses need to be improved. Nonetheless, as the actual SL sample size increases, there will be more lenses identified with smaller Einstein radii, which, as expected, will suffer more from lens light contamination. In a sense, we have addressed the significant effect of lens light contamination and demonstrated the success of the BPL-rigid model in dealing with SL systems with obvious lens light contamination.

There are some simplifications in generating and analyzing the mock images. For example, we do not take into consideration the lensing effects of environment and cosmological large scale structures, which would complicate the data analyses and the lens mass model fittings. We neglect the redshift distributions of foreground lenses and background sources. When applying the B-spline technique to fit the lens light, feature masks are defined automatically by pixels with more than 5% luminosity excess, which in practice cannot be recognized so easily. In the prediction of AL-weighted LOSVDs, the velocity anisotropy parameter is assumed to be constant and known for each lens. These simplifications or assump-

tions may, to some extent, have improved the measurement accuracies of the lens mass distributions or the AL-weighted LOSVDs.

Priors are essential for the BPL model to ensure the accuracy of lens mass reconstructions. We inspect the priors using the Illustris galaxies at a fixed redshift, while the priors are most likely redshift and wavelength dependent. There may exist more precise scaling relations between overall mass and stellar mass (or lens light) distributions. It is thus worthwhile to investigate the priors in more detail.

ACKNOWLEDGMENTS

W.D. acknowledges the support from the National Natural Science Foundation of China (NSFC) under grants 11803043, 11890691 and 11720101004. L.P.F acknowledges the support from NSFC grant 11933002, and the Innovation Program 2019-01-07-00-02-E00032 of SMEC. Y.S. acknowledges the support from the China Manned Spaced (CMS) Project with No. CMS-CSST-

2021-A12. R.L. acknowledges the support by National Key R&D Program of China (No. 2022YFF0503403), the support of NSFC (Nos. 11988101 and 12022306), the support from the Ministry of Science and Technology of China (No. 2020SKA0110100), CAS Project for Young Scientists in Basic Research (No. YSBR-062), and the support from K.C.Wong Education Foundation. Z.H.F is supported by NSFC under grants 11933002 and U1931210. C.G.S. acknowledges the support by NSFC under grant No. 12141302, and the Science and Technology Commission of Shanghai Municipality (STCSM No. 22590780100). We acknowledge the science research grants from the CMS Project with Nos. CMS-CSST-2021-A01 and CMS-CSST-2021-B01. We would like to thank the Laohu high-performance computing (HPC) cluster supported by National Astronomical Observatories, Chinese Academy of Sciences, which was utilized for part of the MCMC runs. The authors also acknowledge Beijing PARATERA Tech CO., Ltd. (<https://www.paratera.com/>) for providing HPC resources that have contributed to the research results reported within this paper.

REFERENCES

Birrer, S., Shajib, A. J., Galan, A., et al. 2020, *A&A*, 643, A165

Birrer, S. 2021, *ApJ*, 919, 38

Bolton, A. S., Burles, S., Koopmans, L. V. E., Treu, T., & Moustakas, L. A. 2006, *ApJ*, 638, 703

Bolton, A. S., Rappaport, S., & Burles, S. 2006, *PhRvD*, 74, 061501

Bolton, A. S., Burles, S., Koopmans, L. V. E., et al. 2008, *ApJ*, 682, 964

Bonvin, V., Courbin, F., Suyu, S. H., et al. 2017, *MNRAS*, 465, 4914

Bottrell, C., Torrey, P., Simard, L., et al. 2017, *MNRAS*, 467, 2879

Bourassa, R. R., & Kantowski, R. 1975, *ApJ*, 195, 13

Bray, I. 1984, *MNRAS*, 208, 511

Cao, S., Biesiada, M., Gavazzi, R., et al. 2015, *ApJ*, 806, 185

Cao, X., Li, R., Nightingale, J. W., et al. 2022, *Research in Astronomy and Astrophysics*, 22, 025014

Chabrier, G. 2003, *PASP*, 115, 763

Chen, G. C.-F., Fassnacht, C. D., Suyu, S. H., et al. 2022, *MNRAS*, 513, 2349

Ciotti, L., & Bertin, G. 1999, *A&A*, 352, 447

Coe, D., Umetsu, K., Zitrin, A., et al. 2012, *ApJ*, 757, 22

Collett, T. E., Auger, M. W., Belokurov, V., et al. 2012, *MNRAS*, 424, 2864

Collett, T. E., Oldham, L. J., Smith, R. J., et al. 2018, *Science*, 360, 1342

Du, W., Zhao, G.-B., Fan, Z., et al. 2020, *ApJ*, 892, 62

Einasto, J. 1965, *Trudy Astrofizicheskogo Instituta Alma-Ata*, 5, 87

Etherington, A., Nightingale, J. W., Massey, R., et al. 2022, *MNRAS*, 517, 3275

Falco, E. E., Gorenstein, M. V., & Shapiro, I. I. 1985, *ApJL*, 289, L1

Foreman-Mackey, D., Hogg, D. W., Lang, D., et al. 2013, *PASP*, 125, 306

Gebhardt, K., Bender, R., Bower, G., et al. 2000, *ApJL*, 539, L13

Genel, S., Vogelsberger, M., Springel, V., et al. 2014, *MNRAS*, 445, 175

Gomer, M. & Williams, L. L. R. 2020, *JCAP*, 2020, 045

Gorenstein, M. V., Falco, E. E., & Shapiro, I. I. 1988, *ApJ*, 327, 693

Guimarães, A. C. C. & Sodré, L. 2011, *ApJ*, 728, 33

Häring, N. & Rix, H.-W. 2004, *ApJL*, 604, L89

Hockney, R.W.,& Eastwood, J.W. 1981, *Computer Simulations Using Particles* (New York: McGraw-Hill)

Jullo, E., Natarajan, P., Kneib, J.-P., et al. 2010, *Science*, 329, 924

Kassiola, A., & Kovner, I. 1993, *ApJ*, 417, 450

Keeton, C. R., & Kochanek, C. S. 1998, *ApJ*, 495, 157

Keeton, C. R. 2001, astro-ph/0102341

Kochanek, C. S. 2020, MNRAS, 493, 1725

Kochanek, C. S. 2021, MNRAS, 501, 5021

Koopmans, L. V. E., Barnabe, M., Bolton, A., et al. 2009, astro2010: The Astronomy and Astrophysics Decadal Survey, 2010, 159

Kormendy, J. & Ho, L. C. 2013, ARA&A, 51, 511

Li, R., Li, H., Shao, S., et al. 2019, MNRAS, 490, 2124

Liesenborgs, J. & De Rijcke, S. 2012, MNRAS, 425, 1772

Lima Neto, G. B., Gerbal, D., & Márquez, I. 1999, MNRAS, 309, 481

Linder, E. V. 2016, PhRvD, 94, 083510

Luhtaru, R., Schechter, P. L., & de Soto, K. M. 2021, ApJ, 915, 4

Márquez, I., Lima Neto, G. B., Capelato, H., et al. 2001, A&A, 379, 767

MacArthur, L. A., Courteau, S., & Holtzman, J. A. 2003, ApJ, 582, 689

Mao, S., Witt, H. J., & Koopmans, L. V. E. 2001, MNRAS, 323, 301

Marshall, P. J., Treu, T., Melbourne, J., et al. 2007, ApJ, 671, 1196

Millon, M., Galan, A., Courbin, F., et al. 2020, A&A, 639, A101

Navarro, J. F., Frenk, C. S., & White, S. D. M. 1997, ApJ, 490, 493

Nelson, D., Pillepich, A., Genel, S., et al. 2015, Astronomy and Computing, 13, 12

Newton, E. R., Marshall, P. J., Treu, T., et al. 2011, ApJ, 734, 104

Mukherjee, S., Koopmans, L. V. E., Metcalf, R. B., et al. 2018, MNRAS, 479, 4108

O'Riordan, C. M., Warren, S. J., & Mortlock, D. J. 2021, MNRAS, 501, 3687

Reines, A. E. & Volonteri, M. 2015, ApJ, 813, 82

Saha, P. 2000, AJ, 120, 1654

Schaye, J., Crain, R. A., Bower, R. G., et al. 2015, MNRAS, 446, 521

Schneider, P., & Sluse, D. 2013, A&A, 559, A37

Schneider, P. & Sluse, D. 2014, A&A, 564, A103

Schneider P., Kochanek C. & Wambsganss J. 2006, Gravitational Lensing: Strong, Weak and Micro, Springer-Verlag Berlin Heidelberg

Schwab, J., Bolton, A. S., & Rappaport, S. A. 2010, ApJ, 708, 750

Shajib, A. J., Birrer, S., Treu, T., et al. 2019, MNRAS, 483, 5649

Shajib, A. J., Birrer, S., Treu, T., et al. 2020, MNRAS, 494, 6072

Shajib, A. J., Treu, T., Birrer, S., et al. 2021, MNRAS, 503, 2380

Shu, C., Zhou, B., Bartelmann, M., et al. 2008, ApJ, 685, 70

Shu, Y., Bolton, A. S., Brownstein, J. R., et al. 2015, ApJ, 803, 71

Shu, Y., Bolton, A. S., Mao, S., et al. 2016, ApJ, 833, 264

Sijacki, D., Vogelsberger, M., Genel, S., et al. 2015, MNRAS, 452, 575

Sonnenfeld, A. 2018, MNRAS, 474, 4648

Suyu, S. H., Marshall, P. J., Auger, M. W., et al. 2010, ApJ, 711, 201

Suyu, S. H., Auger, M. W., Hilbert, S., et al. 2013, ApJ, 766, 70

Terzić, B., & Graham, A. W. 2005, MNRAS, 362, 197

Tessore, N., & Metcalf, R. B. 2015, A&A, 580, A79

Tikhonova, O., Courbin, F., Harvey, D., et al. 2020, MNRAS, 498, 1406

Treu, T., Gavazzi, R., Gorecki, A., et al. 2009, ApJ, 690, 670

Treu, T. 2010, ARA&A, 48, 87

Unruh, S., Schneider, P., & Sluse, D. 2017, A&A, 601, A77

Vogelsberger, M., Genel, S., Springel, V., et al. 2014, MNRAS, 444, 1518

Wagner, J. 2018, A&A, 620, A86

Wertz, O., & Surdej, J. 2014, MNRAS, 437, 1051

Wong, K. C., Suyu, S. H., Chen, G. C.-F., et al. 2020, MNRAS, 498, 1420

Xu, D., Sluse, D., Schneider, P., et al. 2016, MNRAS, 456, 739

Xu, D., Springel, V., Sluse, D., et al. 2017, MNRAS, 469, 1824